

CGC/saturation approach: Impact-parameter dependent model in next-to-leading order of perturbative QCD and combined HERA data

Michael Sanhueza,^{1,2,*} José Garrido,^{3,†} and Miguel Guevara^{1,‡}

¹*Facultad de Ingeniería, Laboratorio DataScience,*

Universidad de Playa Ancha, Leopoldo Carvallo 270, Valparaíso, Chile

²*Centro de Estudios Avanzados, Universidad de Playa Ancha, Traslaviña 450, Viña del Mar, Chile*

³*Departamento de Física, Universidad Técnica Federico Santa María,
Avenida España 1680, Casilla 110-V, Valparaíso, Chile*

In this paper we confront the next-to-leading order (NLO) CGC/saturation approach of Ref. [1] with the experimental combined HERA data and obtain its parameters. The model includes two features that are in accordance with our theoretical knowledge of deep inelastic scattering. These consist of: *i*) the use of analytical solution for the non-linear Balitsky-Kovchegov (BK) evolution equation and *ii*) the exponential behavior of the saturation momentum on the impact parameter b -dependence, characterized by $Q_s \propto \exp(-mb)$ which reproduces the correct behavior of the scattering amplitude at large b in accord with Froissart theorem. The model results are then compared to data at small- x for the structure-function of the proton F_2 , the longitudinal structure function F_L , the charm structure function $F_2^{c\bar{c}}$, the exclusive vector meson ($J/\psi, \phi, \rho$) production and Deeply Virtual Compton Scattering (DVCS). We obtain a good agreement for the processes in a wide kinematic range of Q^2 at small x . Our results provide a strong guide for finding an approach, based on Color Glass Condensate/saturation effective theory for high energy QCD, to make reliable predictions from first principles and for forthcoming experiments like the Electron-Ion Collider and the LHeC.

PACS numbers: 12.38.Cy, 12.38g, 24.85.+p, 25.30.Hm

I. INTRODUCTION

The goal of this paper is to confront the next-to-leading order (NLO) Color Glass Condensate (CGC)/saturation approach of Ref. [1] with the experimental combined HERA data and obtain its parameters via fit. In order to contrast with experimental data, it was selected deep inelastic processes using the CGC/saturation equations from Ref.[2] in a simple version of the non-linear Balitsky-Kovchegov (BK) equation [3]. The authors of Ref. [1] proposed a way to take into account the NLO corrections, which coincides with other attempts on the market, as far as the linear dynamics is concerned, but introduce the non-linear evolution which guarantees the correct high energy asymptotic behavior of the scattering amplitude. They include the re-summation procedure suggested in Refs. [4–6], to fix the BFKL kernel in the NLO. Specifically, the rapidity variable was introduced in the same way as in Ref. [7]. Nevertheless, a different way to account the non-linear corrections was suggested which leads to additional change of the NLO kernel of the evolution equation. The advantage of the BFKL kernel [8, 9], is that it leads to the scattering amplitude satisfying high-energy limits, which follows from the approach of Ref. [10] (see Refs. [11, 12]) concerning to the NLO-BK [3] evolution equation [13–19].

It is widely accepted that finding the correct NLO approximation for the nonlinear evolution is one of the most important and urgent problem in the theoretical understanding of high energy scattering, since the BFKL Pomeron intercept is too large leaving the theoretical estimates in severe qualitative contradiction with experimental data. In fact, the two essential parameters that determine the high energy scattering are the BFKL Pomeron [8] intercept, which is equal to $2.8\bar{\alpha}_S$, and leads to the energy behavior of the scattering amplitude $N \propto \exp(2.8\bar{\alpha}_S \ln(\frac{1}{x}))$ and the energy behavior of the saturation momentum $Q_s^2 \propto \exp(4.88\bar{\alpha}_S \ln(\frac{1}{x}))$. Both scenarios show an increase in the leading order CGC approach, which is inconsistent with the existing experimental data. Hence, the large NLO corrections remain the singular path forward, now as well as two decades ago. In Ref. [1] it was found the analytical solution of the nonlinear BK equation taking into account the main features of the NLO corrections to the BFKL kernel such is able to describe the experimental HERA data.

The model which is based on CGC/saturation effective theory for high energy QCD (see Ref. [20] for a review), includes the impact parameter dependence of the scattering amplitude. Within this framework, the scattering amplitude falls down at large impact parameters b as a power of b . Such a power-like decrease leads to the violation of the Froissart theorem [21]. Therefore, we have no choice but to build a model because CGC/saturation equations cannot reproduce the correct behavior of the scattering amplitude at large impact parameters [22, 23]. In accordance with the geometric scaling behavior of the scattering amplitude [24, 25] and guided by the semi-classical solution

to the CGC/saturation equations [26], this approach incorporates the non-perturbative impact parameter behavior into the saturation momentum. In most cases, these models include the non-perturbative b -behavior of the scattering amplitude and has been widely applied in what is commonly referred to as saturation models [11, 27–48]. In the choice of the nonperturbative behavior of the saturation scale, instead to use the common approach proportional to $\exp(-b^2/B)$ which disagrees the theoretical knowledge of QCD at high energies [10, 21], we will parametrize as follows [11, 47, 48]:

$$Q_s^2(b, Y) \propto (S(b, m))^{\frac{1}{\bar{\gamma}}} \quad (1)$$

where $S(b)$ is the Fourier image of $S(Q_T) = 1/\left(1 + \frac{Q_T^2}{m^2}\right)^2$ and the value of $\bar{\gamma}$ we will discuss in section III. In the vicinity of the saturation scale, this b dependency leads to a significant b -dependence of the scattering amplitude, which is proportional to $\exp(-mb)$ for $b \gg 1/m$, consistent with the Froissart theorem [21]. We want to stress the fact that the model's b -dependence is congruent with perturbative QCD calculations for large values of momentum transferred (Q_T), leading to a power-like behavior in the scattering amplitude at high Q_T [49].

Based on these observations and remarks, this paper undertakes an examination of how the CGC/saturation NLO dipole model reproduces the combined HERA data and conducts a detailed analysis thereof. Furthermore, the combined data for inclusive deep inelastic scattering (DIS) have been measured with high accuracy by H1 and ZEUS collaboration [50, 51] featuring extremely small error bars. This characteristic underscores the substantial challenge faced by any theoretical approach in accurately describing this data. Fitting the model to this data allows us to extract all phenomenological parameters that are introduced in the model. After determining the values of all phenomenological free parameters we calculated and compared the theoretical results with experimental data at small- x for several observables, including the proton structure function F_2 , the longitudinal structure function F_L , the charm structure function $F_2^{c\bar{c}}$, as well as exclusive vector meson production ($J/\psi, \phi, \rho$) and Deeply Virtual Compton Scattering (DVCS).

Our results provide a strong guide in the continuous process for finding an approach, based on Color Glass Condensate/saturation effective theory for high energy QCD, to make reliable predictions from first principles, as well as for forthcoming experiments like the Electron-Ion Collider [52] and the LHeC [53]. Another important application is to use the dipole amplitude for the production of dijets in p-p and p-Pb collisions [54] or the structure of the soft Pomeron in CGC [55]. This paper is organized as follows. In section II, we present a brief overview of the framework for computing the total DIS cross-section, structure functions, and exclusive diffractive processes within the color dipole approach. In section III, we specify the approach of the CGC/saturation NLO dipole model, presenting the main formulation employed for describing the experimental data. Specifically, we introduce the phenomenological parameters that need to be calculated within the nonperturbative QCD framework. Section IV is dedicated to discussing the numerical results obtained from our analysis. Finally, we summarize our results in the conclusion.

II. DESCRIPTION OF INCLUSIVE AND EXCLUSIVE DIFFRACTIVE PROCESSES

A. Inclusive processes: Total DIS cross-section and proton structure functions

The observables in deep inelastic scattering (DIS) can be expressed through the following scattering amplitudes (see Ref. [20] and references therein):

$$N_{L,T}(Q, Y; b) = \int \frac{d^2r}{4\pi} \int_0^1 dz |\Psi_{L,T}^{\gamma^*}(Q, r, z)|^2 N(r, Y; b) \quad (2)$$

where $Y = \ln(1/x_{Bj})$ and x_{Bj} is the Bjorken x . z is the fraction of the light cone momentum of the virtual photon carried by quark. Q is the photon virtuality and L, T denote the longitudinal and transverse polarizations of the virtual photon. In the dipole picture of DIS at high energies, the interactions are characterized by the features shown in Eq. (2). The process occurs as follows: in the first stage the virtual photon decay into quark-antiquark pair, described by $|\Psi_{L,T}^{\gamma^*}(Q, r, z)|^2$. During the second stage, the color dipole proceeds to interact with the target (proton) represented by $N(r, Y; b)$, which is the imaginary part of the forward $q\bar{q}$ dipole-proton scattering amplitude with transverse dipole size r and impact parameter b .

The wave function for $|\Psi_{L,T}^{\gamma^*}(Q, r, z)|^2 \equiv (\Psi^* \Psi)_{L,T}^{\gamma^*}$ is well known (see Ref. [20] and references therein).

$$(\Psi^* \Psi)_T^{\gamma^*} = \frac{2N_c}{\pi} \alpha_{\text{e.m.}} \sum_f e_f^2 \{ [z^2 + (1-z)^2] \epsilon_f^2 K_1^2(\epsilon_f r) + m_f^2 K_0^2(\epsilon_f r) \}, \quad (3)$$

$$(\Psi^* \Psi)_L^{\gamma^*} = \frac{8N_c}{\pi} \alpha_{\text{e.m.}} \sum_f e_f^2 Q^2 z^2 (1-z)^2 K_0^2(\epsilon_f r), \quad (4)$$

with

$$\epsilon_f^2 = m_f^2 + z(1-z)Q^2 \quad (5)$$

where $\alpha_{\text{e.m.}}$ is the electromagnetic fine structure constant, N_c denotes the number of colors and e_f is the electric charge of a quark with flavor f and mass m_f . In $c\bar{c}$ scattering, the mass of the charm quark (about $m_c = 1.4 \text{ GeV}$) is not small and we took this into account by replacing x as $x_c = x_{Bj}(1 + 4m_c^2/Q^2)$. Using Eq. (2), Eq. (3) and Eq. (4) we can write the main observables in DIS as follows:

$$\sigma_{T,L}^{\gamma^* p}(Q^2, x) = 2 \int d^2b N_{T,L}(Q, Y; b); \quad (6a)$$

$$F_2(Q^2, x) = \frac{Q^2}{4\pi^2 \alpha_{\text{e.m.}}} [\sigma_T^{\gamma^* p}(Q^2, x) + \sigma_L^{\gamma^* p}(Q^2, x)]; \quad (6b)$$

$$F_2^{c\bar{c}}(Q^2, x) = \frac{Q^2}{4\pi^2 \alpha_{\text{e.m.}}} [\sigma_T^{c\bar{c}, \gamma^* p}(Q^2, x) + \sigma_L^{c\bar{c}, \gamma^* p}(Q^2, x)]; \quad (6c)$$

$$F_L(Q^2, x) = \frac{Q^2}{4\pi^2 \alpha_{\text{e.m.}}} \sigma_L^{\gamma^* p}(Q^2, x); \quad (6d)$$

The reduced cross-section σ_r is expressed in terms of the inclusive proton structure functions F_2 and F_L as

$$\sigma_r(Q^2, x, y) = F_2(Q^2, x) - \frac{y^2}{1 + (1-y)^2} F_L(Q^2, x) \quad (7)$$

where $y = Q^2/(sx)$ denotes the inelasticity variable and \sqrt{s} indicates the center of mass energy in ep collisions.

B. Exclusive diffractive processes: Deeply virtual Compton scattering and exclusive vector meson production

In the dipole approach, the scattering amplitude for the exclusive diffractive processes $\gamma^* + p \rightarrow E + p$, with the final state a real photon $E = \gamma$ in DVCS or vector meson $E = J/\psi, \phi, \rho$ can be written in terms of a convolution of the dipole amplitude N and the overlap wave functions of the photon and the exclusive final-state particle. The main formula for exclusive diffractive processes takes the form [35]:

$$\mathcal{A}_{T,L}^{\gamma^* p \rightarrow Ep}(x, Q, \Delta) = 2i \int d^2\mathbf{r} \int_0^1 \frac{dz}{4\pi} \int d^2\mathbf{b} (\Psi_E^* \Psi)_{T,L} e^{-i[\mathbf{b} - (\frac{1}{2}-z)\mathbf{r}] \cdot \Delta} N(r, Y; b) \quad (8)$$

where $|\Delta|^2 = -t$, and t represents the squared momentum transfer. The phase factor $\exp(i(\frac{1}{2}-z)\mathbf{r} \cdot \Delta)$ is due to the non-forward wave-functions contribution [56], with the correct phase factor of $\frac{1}{2}$ found in [57].

In terms of the scattering amplitude of Eq. (8), the differential cross-section for exclusive diffractive processes may be written as [32, 35]

$$\frac{d\sigma_{T,L}^{\gamma^* p \rightarrow Ep}}{dt} = \frac{1}{16\pi} \left| \mathcal{A}_{T,L}^{\gamma^* p \rightarrow Ep} \right|^2 (1 + \beta^2) \quad (9)$$

where

$$\sigma_{T,L}^{\gamma^* p \rightarrow Ep} = \int dt \frac{d\sigma_{T,L}^{\gamma^* p \rightarrow Ep}}{dt} \quad (10)$$

and

$$B_D = \lim_{t \rightarrow 0} \frac{d}{dt} \ln \left(\frac{d\sigma_{T,L}^{\gamma^* p \rightarrow Ep}}{dt} \right) \quad (11)$$

are the two main observables that we are going to use to calculate our theoretical estimates. In order to account for the missing real part of Eq. (8), a multiplicative factor $(1 + \beta^2)$ must be added, where β is the ratio of the real to imaginary parts of the scattering amplitude which shows Regge-type behavior at high energies [58–60]

$$\beta = \tan(\pi\delta/2), \quad \text{with } \delta \equiv \frac{\partial \ln(\mathcal{A}_{T,L}^{\gamma^* p \rightarrow Ep})}{\partial \ln(1/x)} \quad (12)$$

It is worth mentioning that for exclusive diffractive processes, it becomes imperative to consider the skewedness effect. This arises since the gluons attached to the $q\bar{q}$ pair can carry distinct light-cone fractions x, x' of the proton. At the NLO level, particularly under the condition where $x' \ll x \ll 1$, the skewedness effect [61] can be accounted by simply multiplying the gluon distribution $xg(x, \mu^2)$ by a factor R_g defined via

$$R_g = \frac{2^{2\gamma+3} \Gamma(\gamma + 5/2)}{\sqrt{\pi} \Gamma(\gamma + 4)}, \quad \text{with } \gamma \equiv \frac{\partial \ln[xg(x, \mu^2)]}{\partial \ln(1/x)} \quad (13)$$

For deeply virtual Compton scattering (DVCS) the overlap wave function only has transversal contribution. Similar to Eq. (3) where a sum over quark flavors should be done, the equation read as

$$(\Psi_\gamma^* \Psi)_T^{(DVCS)} = \frac{2N_c}{\pi} \alpha_{\text{em}} \sum_f e_f^2 \{ [z^2 + (1-z)^2] \epsilon_f K_1(\epsilon_f r) m_f K_1(m_f r) + m_f^2 K_0(\epsilon_f r) K_0(m_f r) \} \quad (14)$$

For vector meson diffractive production, we have wave functions exclusively for mesons composed of heavy quarks. The J/ψ is the most commonly cited example. Nevertheless, it is important to take into account that the charm quark's mass is not very large, and corrections can be crucial. For all other mesons, confinement corrections are substantial, and the wave function, motivated by heavy quark mesons, can only be considered as pure phenomenological assumptions. The overlap integrals are represented according to the prescription from Ref. [33]

$$(\Psi_V^* \Psi)_T = \hat{e}_f e \frac{N_c}{\pi z(1-z)} \{ m_f^2 K_0(\epsilon_f r) \phi_T(r, z) - [z^2 + (1-z)^2] \epsilon_f K_1(\epsilon_f r) \partial_r \phi_T(r, z) \} \quad (15)$$

$$(\Psi_V^* \Psi)_L = \hat{e}_f e \frac{N_c}{\pi} 2Qz(1-z) K_0(\epsilon_f r) \left[M_V \phi_L(r, z) + \frac{m_f^2 - \nabla_r^2}{M_V z(1-z)} \phi_L(r, z) \right] \quad (16)$$

$$\phi_{T,L}(r, z) = \mathcal{N}_{T,L} z(1-z) \exp \left(-\frac{m_f^2 \mathcal{R}^2}{8z(1-z)} - \frac{2z(1-z)r^2}{\mathcal{R}^2} + \frac{m_f^2 \mathcal{R}^2}{2} \right) \quad (17)$$

where $\nabla_r^2 \equiv (1/r)\partial_r + \partial_r^2$, M_V is the meson mass and the effective charge \hat{e}_f takes the values of $2/3$, $1/3$, or $1/\sqrt{2}$ for J/ψ , ϕ , or ρ mesons respectively. The parameters $\mathcal{N}_{T,L}$, \mathcal{R} and m_f are from Table 2 in Ref. [32].

III. CGC/SATURATION NLO DIPOLE MODEL

A. $q\bar{q}$ dipole-proton scattering amplitude

To compute the total cross-section, the proton structure functions in DIS, exclusive diffractive vector meson production, and Deeply Virtual Compton Scattering, we need to use the $q\bar{q}$ dipole-proton forward scattering amplitude. In Ref. [1] the analytical solution for the nonlinear BK equation was found at NLO BFKL kernel in the saturation domain. The authors propose a method to incorporate NLO corrections by introducing non-linear evolution, which ensures the correct high-energy asymptotic behavior of the scattering amplitude. They incorporate the re-summation procedure proposed in Refs. [4–6], to address the BFKL kernel at NLO. Specifically, the rapidity variable was introduced in a similar manner that in Ref. [7]. Nevertheless, a different way to account the non-linear corrections was suggested: the anomalous dimension was derived in the region of large $\tau = r^2 Q_s^2$ in the limit when $\gamma \rightarrow 0$ by using the

kernel in γ -representation for the leading twist in place of the full BFKL kernel (see equation 90 from Ref. [1]), which corresponds to the sum of two types of logarithms [10]. The advantage of the BFKL kernel [8, 9], is that it leads to the scattering amplitude satisfying high-energy limits, which follows from the approach of Ref. [10] (see Refs. [11, 12]) concerning to the NLO-BK [3] evolution equation [13–19].

In the CGC/saturation NLO dipole model, the color $q\bar{q}$ dipole-proton scattering amplitude is given by [1, 48]:

$$N(z) = \begin{cases} N_0 e^{z\bar{\gamma}} & \text{for } \tau \leq 1; \\ a \left(1 - e^{-\Omega(z)}\right) + (1 - a) \frac{\Omega(z)}{1 + \Omega(z)} & \text{for } \tau > 1; \end{cases} \quad (18)$$

The parameter $a = 0.65$ describes the exact solution of the nonlinear BK equation within an accuracy of less than 2.5% [48, 62], while the function $\Omega(z)$ takes the following form according to references [1, 48]:

$$\Omega(z) = \Omega_0 \left\{ \cosh(\sqrt{\sigma}z) + \frac{\bar{\gamma}}{\sqrt{\sigma}} \sinh(\sqrt{\sigma}z) \right\}, \quad \text{with } \sigma = \frac{\bar{\alpha}_S}{\lambda(1 + \bar{\alpha}_S)}; \quad (19)$$

The parameter Ω_0 has the same numerical value as N_0 , ensuring the proper behavior of the solution for Eq. (18). N_0 represents the value of the scattering amplitude at $\tau = 1$ and $\bar{\alpha}_S = N_c \alpha_S / \pi$ where N_c denotes the number of colours. While theoretically, the value of N_0 can be computed using the linear evolution equation with appropriate initial conditions, it inherently relies on the phenomenological parameters of said initial condition. Consequently, we treat N_0 as a parameter to be determined through fitting.

The variable z is defined as

$$z = \ln(r^2 Q_s^2(Y, b)) \quad (20)$$

The use of this variable indicates the main idea of the approach in the region for $\tau = r^2 Q_s^2 > 1$. The goal is to establish a correspondence between the solution of the non-linear equation and the solution of the linear equation in the kinematic region described by $N = N_0 e^{z\bar{\gamma}}$.

The critical anomalous dimension and the energy behavior of the saturation scale were determined in NLO in Ref. [1] which has the following form:

$$\bar{\gamma} = \bar{\gamma}_\eta(1 + \lambda_\eta), \quad \text{with } \bar{\gamma}_\eta = \sqrt{2 + \bar{\alpha}_S} - 1; \quad (21)$$

and

$$\lambda = \frac{\lambda_\eta}{1 + \lambda_\eta}, \quad \text{with } \lambda_\eta = \frac{1}{2} \frac{\bar{\alpha}_S}{(3 + \bar{\alpha}_S - 2\sqrt{2 + \bar{\alpha}_S})}; \quad (22)$$

where $\eta = Y - \xi$ is a new energy variable, with $Y = \ln(1/x)$ the rapidity of the dipole and $\xi = \ln(r^2 Q_s^2(Y = 0, \mathbf{b}))$.

We use a different way to introduce the parameters from the experimental data: expanding the linear solution of Eq. (18) to the region $\tau < 1$, replacing $\bar{\gamma}$ by the following expression:

$$\bar{\gamma} \rightarrow \bar{\gamma} + \frac{\ln(1/\tau)}{2\kappa\lambda Y}, \quad \text{with } \kappa = \frac{\chi''(\bar{\gamma})}{\chi'(\bar{\gamma})} = \frac{\frac{d^2\omega(\bar{\gamma}_\eta)}{d\bar{\gamma}_\eta^2}}{\frac{d\omega(\bar{\gamma}_\eta)}{d\bar{\gamma}_\eta}} \quad (23)$$

this equation was derived in Ref. [63] and the results from saturation models [11, 27, 29–48] demonstrate a strong agreement with the experimental data for $x \leq 0.01$. The eigenvalue of $\omega(\bar{\gamma}_\eta)$ was taken from Ref. [1].

B. Phenomenological input: Impact parameter dependence of the saturation scale

Until now, we have only incorporated one phenomenological parameter: N_0 which determines the scattering amplitude at $r^2 Q_s^2 = 1$. However, we must define the initial conditions at $Y = 0$ for the linear evolution equation in the

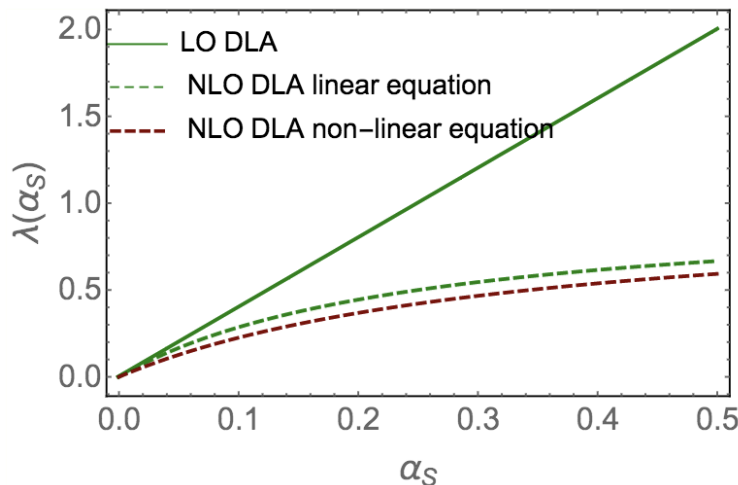


FIG. 1: λ for Y dependence of the saturation scale: $Q_s^2(Y) = Q_s^2(Y=0) \exp(\lambda Y)$ versus $\bar{\alpha}_S$. The solid line corresponds to $\lambda = 4\bar{\alpha}_S$ in LO DLA, dashed green curve describes the NLO DLA value of linear equation and the dashed red curve indicates the NLO DLA value of non-linear equation in the considered kinematic region. The figure was taken from Ref. [1].

region where $\tau = r^2 Q_s^2 \leq 1$. This involves the value of saturation scale at $b = 0$ and how it changes with the impact parameter b . Nevertheless, both aspects are constrained to the non-perturbative realm of QCD, and the current understanding is limited, leading to the suggestion of a phenomenological parameterization. We use the following expression from Refs. [11, 47] to represent the saturation momentum:

$$Q_s^2(Y, b) = Q_s^2(Y=0, b=0) S(b)^{1/\bar{\gamma}} e^{\lambda Y} = Q_0^2 (m b K_1(m b))^{1/\bar{\gamma}} e^{\lambda Y}; \quad (24)$$

This expression leads to $Q_s^2(Y = Y_0, b) \xrightarrow{mb \gg 1} \exp(-mb/\bar{\gamma})$, differs from others by providing the correct large b behavior of the scattering amplitude. The exponential decrease at large b adhering to theoretical principles of analyticity and unitarity [21]. This approach stands in contrast to models from Refs. [34–38, 41, 46] using $Q_s^2(Y = Y_0, b) \propto \exp(-b^2/B)$. How the scattering amplitude behaves at large impact parameter b is critical for understanding how the interaction radius changes with collision energy. According to a fundamental principle (Froisart theorem [21]), b should increase proportionally with Y to ensure the interaction radius has the correct energy dependence. This difference in b -dependence leads to distinct relationships between the interaction radius (R) and Y : with an exponential decrease, R scales as $(1/m)Y$, while a Gaussian decrease results in R scaling as $(1/m)Y$. This distinction results in a rapid increase of the scattering amplitude in this particular parameterization, influencing predictions at high energy. The proposed equation for Q_s^2 gives the amplitude close to the saturation scale, proportional to $S(b)$, and generates the behavior $1/\left(1 + \frac{Q_T^2}{m^2}\right)^2$, where Q_T is the momentum transfer. At large Q_T , the amplitude in the model is proportional to $1/Q_T^4$, in line with perturbative QCD calculations [49], a behavior not reproducible with a Gaussian distribution.

The values of Q_0^2 and m will be determined through a fitting procedure. Previous fitting results have yielded Q_0^2 values ranging from 0.15 to 0.25 GeV², and m values approximately between 0.4 and 0.85 GeV. This range encompasses $m = 0.72$ GeV, which serves as the scale for the electromagnetic form factor of the proton, while $m \approx 0.5$ GeV corresponds to the scale for the so-called gluon mass [11, 47]. λ and $\bar{\gamma}$ are defined using the respective expressions provided in Eq. (21), Eq. (22) and Eq. (23). The value of λ represents the energy dependence of the saturation scale, with the typical value of $\lambda = 0.2$ required for accurate description in DIS data. In the NLO model proposed in Ref. [1], it was demonstrated that for $\bar{\alpha}_S$ close to 0.1, the value of λ is approximately 0.2. Subsequently, in Ref. [48], the model was tested against experimental data with the value of $\bar{\alpha}_S$ treated as a free parameter. Remarkably, the model, even when $\bar{\alpha}_S$ was set to 0.2, consistently reproduced the experimental data. In essence, a freely determined $\bar{\alpha}_S$ from experimental data is essential to establish $\lambda(\bar{\alpha}_S)$ at a level capable of accurately describing HERA data. It is worthwhile mentioning that the NLO corrections to the energy dependence of the saturation momentum give considerable contributions at small values of $\bar{\alpha}_S$. Therefore, we consider $\bar{\alpha}_S$ as the fourth parameter of the model, which we expect $\bar{\alpha}_S \approx 0.10$ according to the predictions in the calculations for NLO in perturbative QCD (see Fig. 1).

In summary, we include three phenomenological parameters originating from the initial conditions, and their values are obtained through the fitting procedure with experimental data.

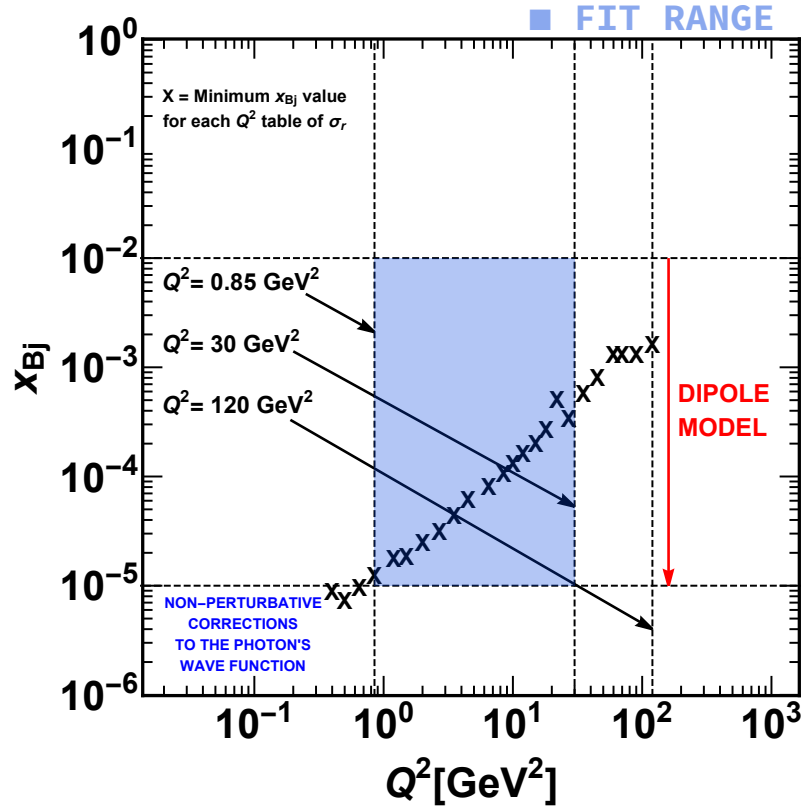


FIG. 2: Fit range in the kinematic plane Q^2 - x_{Bj} . The diagram illustrates two key regions: the non-perturbative range of the photon's wave function ($Q^2 < 0.85 \text{ GeV}^2$) and the domain where the dipole model holds validity ($x < 10^{-2}$). Each marker on the plot represents the minimum x value extracted from experimental data of σ_r within specific Q^2 intervals, compiled from H1 and ZEUS collaborations [50].

IV. NUMERICAL RESULTS AND DISCUSSION

Dipole amplitude				Wave function		Minimization
$\bar{\alpha}_S$	N_0	$Q_0^2 \text{ (GeV}^2\text{)}$	$m \text{ (GeV)}$	$m_{u,d,s} \text{ (GeV)}$	$m_c \text{ (GeV)}$	$\chi^2/\text{d.o.f.}$
$0.1040 \pm 4.6 \times 10^{-4}$	$0.1311 \pm 3.7 \times 10^{-4}$	$0.797 \pm 3.3 \times 10^{-3}$	$0.4743 \pm 9.6 \times 10^{-4}$	$10^{-2} \div 10^{-4}$	1.40	$205.70/166 = 1.239$
$0.1100 \pm 1.8 \times 10^{-4}$	$0.1510 \pm 8.1 \times 10^{-4}$	$0.809 \pm 6.2 \times 10^{-3}$	$0.5412 \pm 1.8 \times 10^{-4}$	$10^{-2} \div 10^{-4}$	1.27	$204.73/166 = 1.233$

TABLE I: Parameters of the CGC/saturation NLO dipole model: $\bar{\alpha}_S$, N_0 , Q_0^2 and m determined through fits to the reduced cross-section σ_r using the combined H1 and ZEUS data [50] within the range $0.85 \text{ GeV}^2 < Q^2 < 30 \text{ GeV}^2$ and $x \leq 10^{-2}$. Results are presented for fixed light quark masses and two fixed values of the charm quark masses (see the text for details).

As we have previously addressed, the model contains four free parameters, which we determine by fitting to experimental data using a χ^2 minimization. We restrict the data used in the fit to reduced inclusive DIS cross-section measurements from the H1 and ZEUS collaborations [50]. Once the parameters are fixed, we compare the theoretical predictions for F_2 , F_L , and $F_2^{c\bar{c}}$ with the experimental HERA data, emphasizing that this data was not included in the fitting process. Importantly, the χ^2 calculation incorporates systematic and statistical uncertainties added in quadrature. Our χ^2 calculation incorporates data within a specific range: $0.85 \text{ GeV}^2 < Q^2 < 30 \text{ GeV}^2$ and $x \leq 10^{-2}$. This choice balances two key factors. First, the validity of the BK equation, upon which our theoretical framework relies, necessitates small- x values. Therefore, we selected a maximum x -value that ensures this condition. Second, we aimed to maximize the data included in the fitting process. The lower Q^2 limit stems from non-perturbative corrections applied to the virtual photon wave function. This choice aligns with our fitting results, which exhibit instability

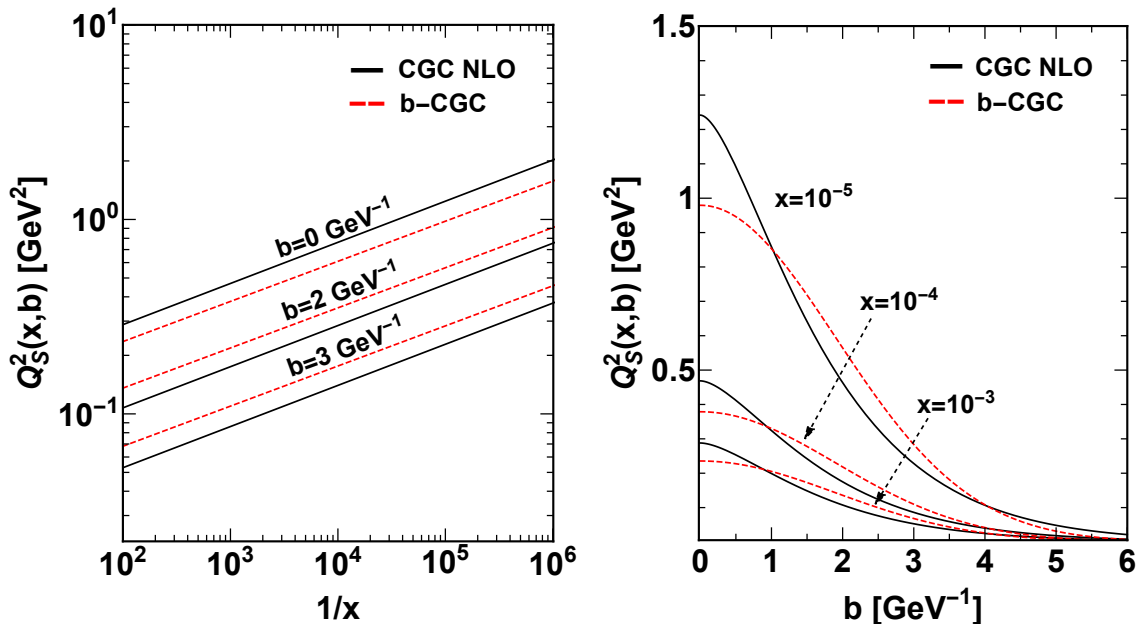


FIG. 3: The left panel displays the saturation scale extracted from the CGC/saturation NLO dipole model, illustrating its variation with $1/x$ for different values of b . In the right panel, the saturation scale is depicted as a function of the impact parameter b for various fixed values of x . Additionally, for comparison, we have included the extracted saturation scale obtained from the b-CGC model [46], utilizing the parameter set with a charm mass of $m_c = 1.27$ GeV for both models.

for Q^2 values below 0.85 GeV². Conversely, the upper Q^2 limit was chosen based on fitting stability. While the fit remains stable within the chosen range (0.85 GeV² $<$ Q^2 $<$ 30 GeV²), it exhibits instability beyond this threshold.

Figure 2 depicts the fitting range within the Q^2 vs x_{Bj} kinematic plane. The illustration delineates the non-perturbative sector of the photon's wave function ($Q^2 < 0.85$ GeV²) as well as the range where the dipole model is applicable ($x < 10^{-2}$). The symbol “X” represents the smallest x -value observed in the experimental data of σ_r within each Q^2 table from the H1 and ZEUS collaborations [50] in the specified kinematic region. The vertical lines represent the range of our fit, $Q^2 \in [0.85, 30]$ GeV², as well as the regions where the observables were predicted. These regions include both the kinematic region defined earlier, as well as regions beyond it, encompassing small values of $Q^2 \leq 0.85$ GeV² and large values of $Q^2 \geq 30$ GeV².

In our analysis, we conducted fits while varying the light quark masses ($m_u = m_d = m_s$) following Refs. [45, 46, 64, 65]. Initially, we employed a fixed value of $m_{u,d,s} = 0.14$ GeV for the light quark masses and subsequently explored a wider range from 10^{-1} to 10^{-4} GeV. This variation encompasses a total of five light quark mass configurations. We further explored the impact of the charm quark mass by considering two fixed values: $m_c = 1.4$ GeV and $m_c = 1.27$ GeV. The resulting $\chi^2/d.o.f.$ values for $m_c = 1.4$ GeV were $\{1.304, 1.312, 1.239, 1.238, 1.239\}$, and for $m_c = 1.27$ GeV were $\{1.354, 1.292, 1.233, 1.234, 1.233\}$. The model exhibited good fit performance for light quark masses in the range of 10^{-2} to 10^{-4} GeV, indicating that the fit becomes stable for current values of quark masses of a few MeV. The model is more sensitive to the mass of the light quarks than to the charm mass during the minimization process. Even when including the $\sigma_r^{c\bar{c}}$ data in our χ^2 calculation, it does not significantly influence the parameter values. However, varying the mass value for the light quarks $m_u = 0.14$ GeV dramatically changes the parameter values, and the χ^2 value varies between 4% and 8% for $m_c = 1.40$ and $m_c = 1.27$, respectively. The resulting values of the free parameters obtained through this fitting process are shown in Table I. One set corresponds to $m_c = 1.40$ GeV, while the other set corresponds to $m_c = 1.27$ GeV.

At the saturation scale, the forward $q\bar{q}$ dipole scattering amplitude N undergoes a rapid increase as x decreases, and the amplitude N becomes significant when non-linear gluon recombination effects turn as prominent as gluon radiation. What differentiates the CGC/saturation NLO dipole model from others is to employ Eq. (24) instead of $Q_s(x,b) \propto \exp(-b^2/B)$ that was used in other saturation models [34–38, 41, 46], which Eq. (24) provide the

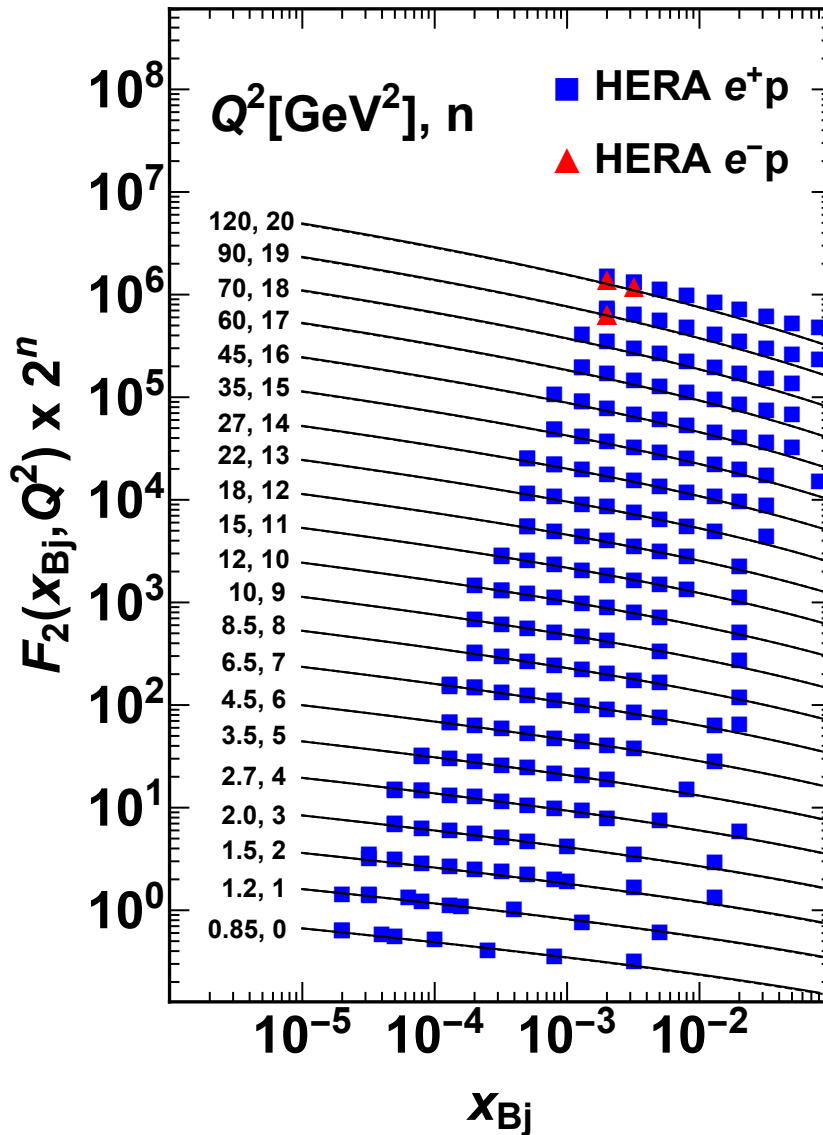


FIG. 4: Theoretical estimates for the structure function $F_2(x, Q^2)$ as a function of x , for different values of Q^2 . The solid and dashed lines are obtained using two distinct sets of parameters from table I corresponding to charm mass values of $m_c = 1.4, 1.27$ GeV, respectively. In order to distinguish each Q^2 from the others, both the theoretical results and the experimental data are multiplied by a factor of 2^n , with the corresponding values of n specified within the plot. The experimental data are from H1 and ZEUS collaborations [50].

correct large b behavior for the scattering amplitude in accord with Froissart theorem [21]. This difference causes the scattering amplitude to increase rapidly in this parametrization, influencing the high-energy predictions significantly. Following Refs. [32, 35, 45, 46], we define the saturation scale $Q_S^2 = 1/r_S^2$, where r_S is the saturation radius, as a scale where the dipole scattering amplitude has a value $N(x, r_S, b) = (1 - \exp(-1/2)) = 0.4^1$. It is worth mentioning that

¹ To ensure the reliability of our results, we incorporate a fixed value of $N(x, r_S, b) = 0.4$ in the formula for comparison with the b-CGC model [46]. It is essential to note that the CGC/saturation NLO dipole model has an additional contribution in the second term of

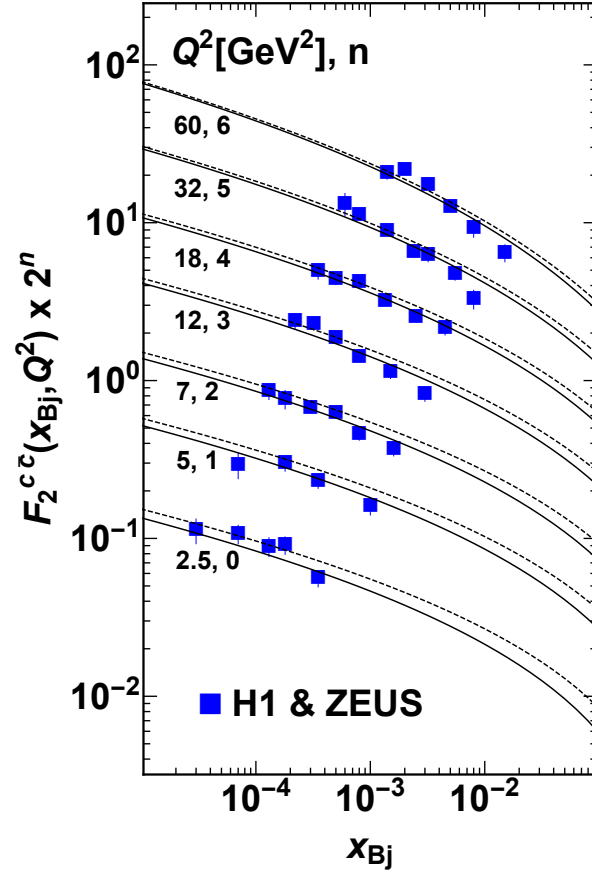


FIG. 5: Results for charm structure function $F_2^{c\bar{c}}(x, Q^2)$ as a function of x , for different values of Q^2 . We used the parameter set I with solid lines ($m_c = 1.4 \text{ GeV}$) and parameter set II with dashed lines ($m_c = 1.27 \text{ GeV}$). The theoretical estimates as well as the experimental data are multiplied by a factor 2^n and the values of n are specified in the plot. The experimental data are from H1 and ZEUS collaboration [51], assuming $\sigma_r^{c\bar{c}} \approx F_2^{c\bar{c}}$ (see the text for explanation).

the saturation scale Q_S^2 differs from the phenomenological parametrization of Eq. (24) with different lower subscript s .

In the left panel of Fig. 3, we depict the saturation scale extracted from both the CGC/saturation NLO dipole model and the b-CGC model [46] as a function of $1/x$ for various impact parameter values b . It is evident that the saturation scale increases more rapidly for collisions with smaller impact parameters, especially those close to central collisions ($b \approx 0$). Additionally, the saturation scale exhibits significant variations across different impact parameter values. This intricate dependence of the saturation scale on the impact parameter highlights its crucial role and needs to be considered for a comprehensive understanding. In the right panel of Fig. 3, which displays the saturation scale as a function of the impact parameter b for several fixed values of x ($x = 10^{-3}, 10^{-4}, 10^{-5}$), we observe that the saturation scale derived from Eq. (24) aligns well with the existing HERA data within the specified x -range ($x \in [10^{-5}, 10^{-2}]$). While the b-CGC model's saturation scale accurately reproduces experimental data, it has limitations in satisfying certain theoretical requirements as discussed in the previous section. Conversely, the saturation scale derived from Eq. (24) fully complies with theoretical considerations. Both scales, within the CGC framework, show similar behaviors, particularly concerning: (i) evolution at small- x and (ii) dependence on the impact parameter b . This dependence includes both the effect of varying b values at a fixed x and the evolution of the b

Eq. (18), which must be taken into account.

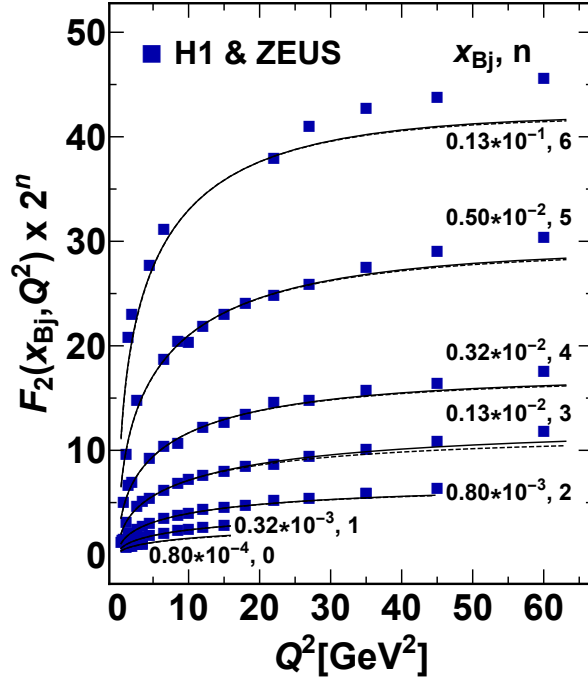


FIG. 6: Results for deep inelastic structure function $F_2(x, Q^2)$ as a function of Q^2 at fixed values of x . The theoretical estimates as well as the experimental data are multiplied by a factor 2^n and the values of x and n are specified in the plot. We use the parameters set given in Table I with $m_c = 1.4 \text{ GeV}$ in solid lines and $m_c = 1.27 \text{ GeV}$ in dashed lines. The experimental data are from H1 and ZEUS collaborations [50].

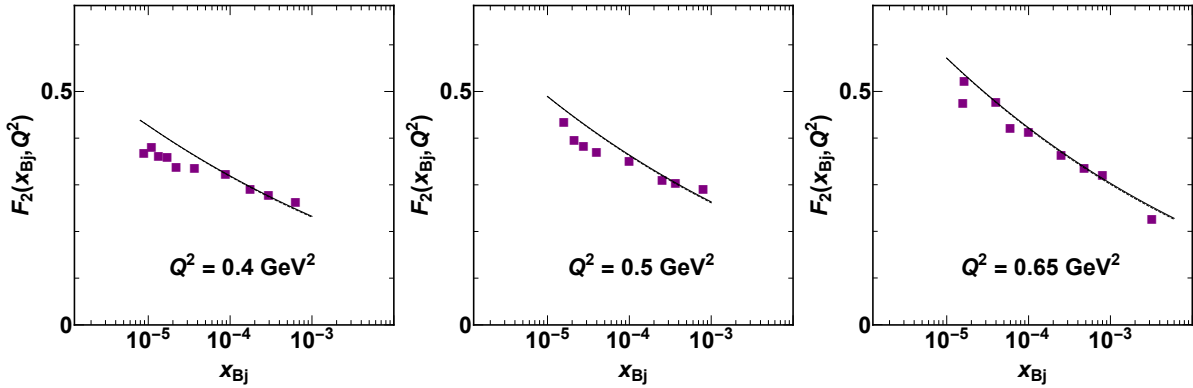


FIG. 7: Results for the structure function $F_2(x, Q^2)$ as a function of x at low values of $Q^2 < 0.85 \text{ GeV}^2$. The solid lines correspond to parameters of set I ($m_c = 1.4 \text{ GeV}$) and the dashed lines correspond to parameters of set II ($m_c = 1.27 \text{ GeV}$). The experimental data are from H1 and ZEUS collaboration [50].

dependence itself with fixed x values.

We only can contrast the model with Refs. [11, 47, 48] since in all other saturation models the assumptions of the saturation scale were made based on Gaussian behavior which contradicts the theoretical information. In Ref. [11], the $\bar{\alpha}_S$ value is within the range $\bar{\alpha}_S \approx 0.14 - 0.15$, whereas in Ref. [48] $\bar{\alpha}_S$ falls in the range $\bar{\alpha}_S \approx 0.09 - 0.04$, and in this paper we have found $\bar{\alpha}_S \approx 0.10 \div 0.11$. As we have discussed previously we have obtained $\lambda \approx 0.20$, and this parameter is essential for determining the energy dependence of the saturation scale which is necessary to describe HERA data. The value of Q_0^2 found via χ^2 is smaller than in Ref. [11] and Ref. [48]. Furthermore, the value of

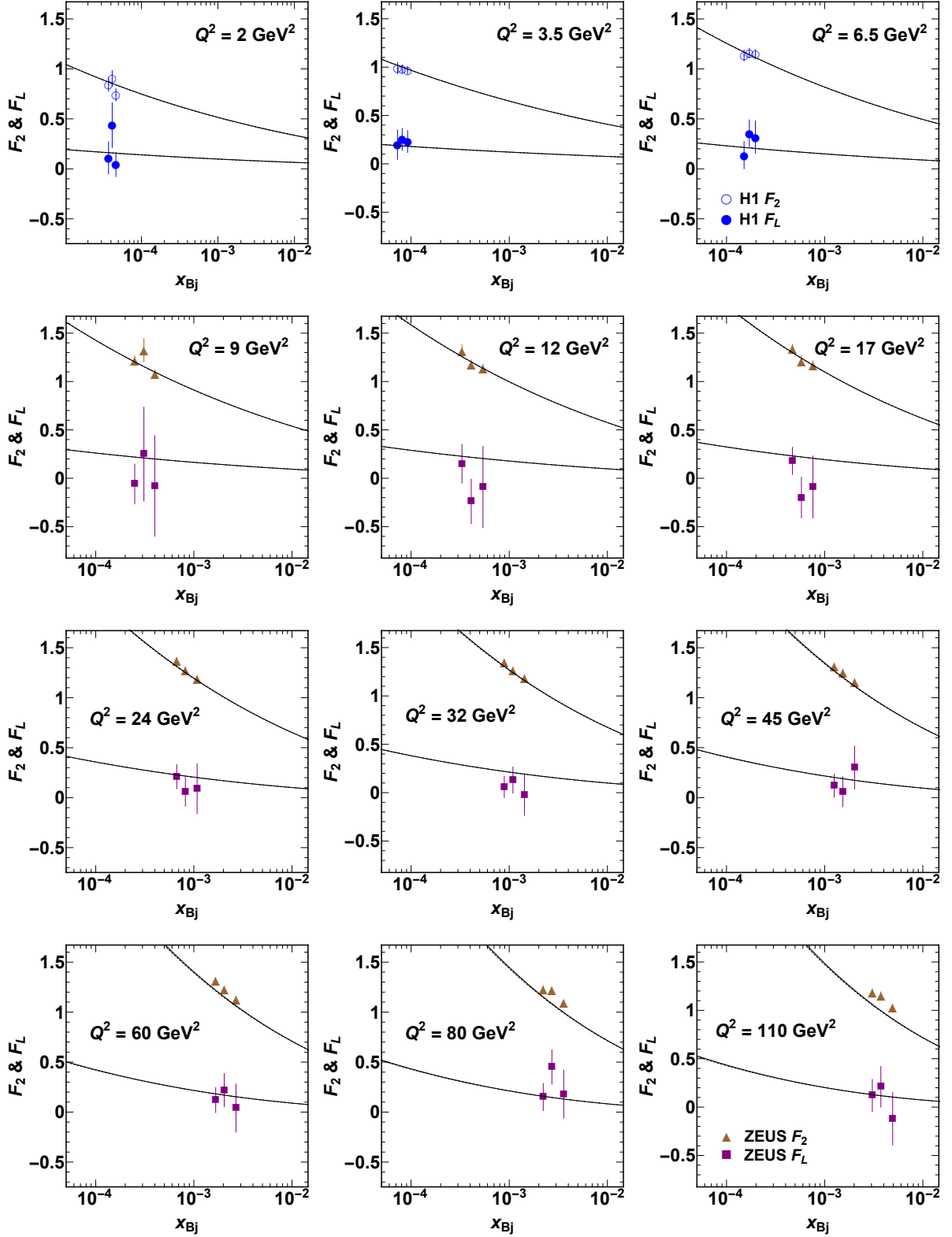


FIG. 8: Results for the longitudinal structure function $F_L(x, Q^2)$ and the structure function $F_2(x, Q^2)$, as functions of x , for different values of Q^2 . The solid and dashed lines are generated using parameter sets from table I, which correspond to charm masses of $m_c = 1.4 \text{ GeV}$ and $m_c = 1.27 \text{ GeV}$, respectively. The experimental data are from ZEUS and H1 collaboration [66, 67].

Inclusive Processes	χ^2
F_2 vs x_{Bj}	1.17
$F_2^{c\bar{c}}$ vs x_{Bj}	1.13
F_2 vs Q^2	1.10
F_2 vs x_{Bj} for low Q^2	4.87
F_2 & F_L vs x_{Bj}	0.87

TABLE II: The χ^2 values corresponding to each plot for inclusive processes, where each plot confronts theoretical results against experimental data from Figure 5 to Figure 9.

$\gamma^*p \rightarrow J/\psi p$	χ^2	$\gamma^*p \rightarrow \phi p$	χ^2	$\gamma^*p \rightarrow \rho p$	χ^2	$\gamma^*p \rightarrow \gamma p$	χ^2
σ vs Q^2	0.33	σ vs Q^2	2.48	σ vs Q^2	0.71	σ vs Q^2	2.23
σ vs W	0.44	σ vs W	2.80	σ vs W	0.85	σ vs W	2.38
R vs Q^2	0.18	R vs Q^2	0.23	R vs Q^2	3.52	B_D vs Q^2	3.33
R vs W	0.58	R vs W	0.41	R vs W	0.51	B_D vs W	4.50
B_D vs Q^2	5.21	B_D vs Q^2	0.65	B_D vs Q^2	0.19	-----	-

TABLE III: The χ^2 values corresponding to each figure depicting exclusive processes, where every graph confronts the theoretical estimates against experimental data from Figure 10 to Figure 16.

m obtained during the χ^2 calculation is closer to the scale of the gluon mass [11, 47]. However, it is important to emphasize a simple distinction between this model and the b-CGC model [46]: the absence of an impact parameter profile for the saturation scale to adjust the slope of the t -distribution in diffractive production. Instead, this behavior is governed by the parameter m , presenting a greater challenge for this model in accurately reproducing experimental data for diffractive processes. Alternatively, one could view this as an advantage of the model, as it only requires four parameters instead of five².

With the parameters extracted from the χ^2 calculation to the reduced inclusive DIS cross-section σ_r , as presented in Table I, we now proceed to compute the proton structure function F_2 , the longitudinal structure function F_L , and the charm structure function $F_2^{c\bar{c}}$. We employ Eqs. (6b), (6c), (6d), and (18) for these computations and then compare them to the combined HERA data sets. The quality of the fit can be observed in Fig. 4. Additionally, we expand our theoretical estimates to high Q^2 values, showing a significant agreement with the data. It is important to note that in this specific kinematic region ($Q^2 > 30 \text{ GeV}^2$), neither F_L nor $F_2^{c\bar{c}}$ were included in the fitting process, making them predictions of the CGC/saturation NLO dipole model. As depicted in Figures 4, 5, 6 and 8 it is clear that the NLO dipole model results exhibit strong agreement with the data on structure functions, over a wide kinematic range: for $Q^2 \in [0.85, 120] \text{ GeV}^2$. Additionally, we have included in Table II the χ^2 values for each plot of the inclusive processes, covering from Figure 4 to Figure 8. The model demonstrates evident consistency with the data, particularly regarding the structure functions F_2 and $F_2^{c\bar{c}}$, with χ^2 values of 1.17 and 1.13, respectively, known for their higher precision in experimental data. For the structure functions F_2 , the agreement with the data remains robust even for $x > 10^{-2}$ (a kinematic range beyond the scope of the dipole model, see figure 2) and only begins to weaken as we approach to $x \approx 10^{-1}$. This consistency can also be taken as a non-trivial test of the model's accuracy, stemming from the two critical parameters governing high-energy scattering: the BFKL Pomeron intercept and the energy behavior of the saturation momentum. Consequently, the theoretical results align well with available experimental data.

When comparing theoretical results with data for the structure-function F_L from the ZEUS and H1 collaborations [66, 67], Fig. 8 demonstrates excellent agreement between the model and data ($\chi^2 = 0.87$) within the specified kinematic range (see Fig. 2) using the two-parameter sets from Table I. Nevertheless, more accurate measurements of

² The b-CGC model [46] boasts four freely adjustable parameters obtained by fitting reduced sigma data. However, a fifth parameter exists, and unlike the others, it is not freely adjusted. Instead, it was fixed by fitting exclusive J/ψ photoproduction data. This separation prevents a high correlation between B_{CGC} and other DIS model parameters, a correlation that can lead to significant instabilities in calculations. In contrast to b-CGC model, the NLO dipole model suffers from a strong correlation between its four free parameters. Further research is required to address the high correlation between the four free parameters in the CGC/saturation NLO dipole model. One approach could be to introduce a fifth parameter, similar to the b-CGC model, and set it by fitting exclusive data of a vector meson like J/ψ . This approach has the potential to mitigate the correlation issue. Alternatively, the existing parameter, m , could be improved by fitting separately to exclusive photoproduction data.

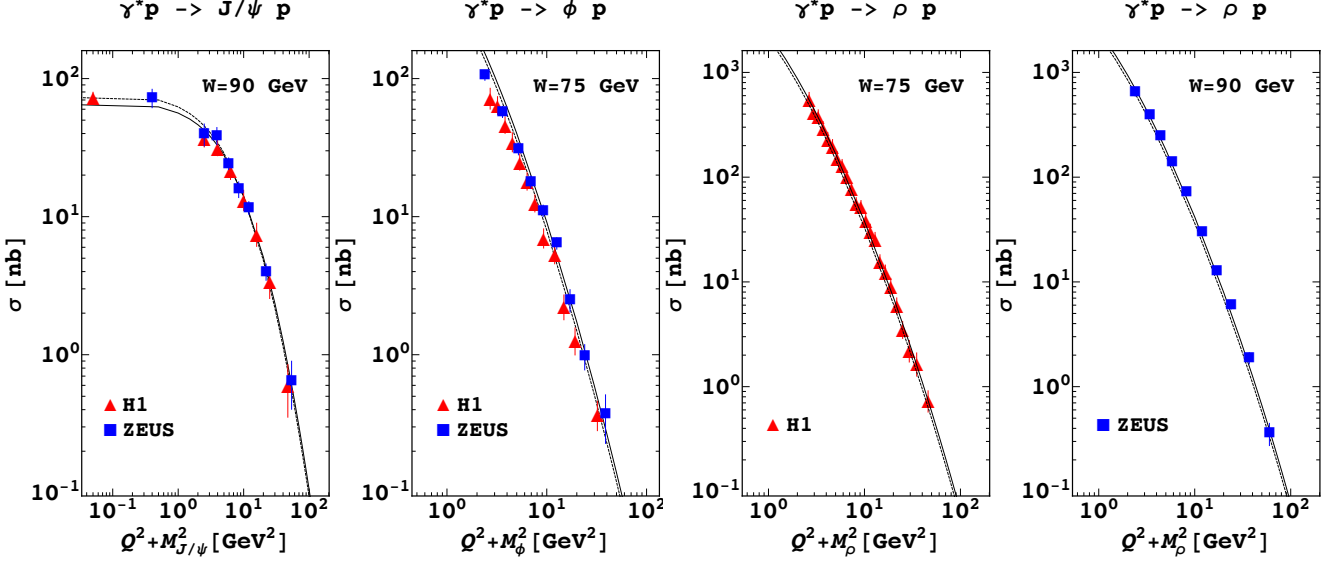


FIG. 9: Total vector meson cross-sections σ for J/ψ , ϕ and ρ , as a function of $Q^2 + M_V^2$ compared to theoretical estimates from CGC/saturation NLO dipole model where solid ($m_c = 1.4 \text{ GeV}$) and dashed ($m_c = 1.27 \text{ GeV}$) lines correspond to parameters of set I and set II, respectively. The data are from H1 and ZEUS collaborations [69–75].

F_L data are required. In Figs. 4, 5, and 8 we extend our theoretical results outside the kinematics of existing data, offering insights for future DIS experiments. Fig. 5 illustrates the F_2^{cc} data under the assumption that $\sigma_r^{cc} \approx F_2^{cc}$. It is important to note that the contribution of F_L^{cc} to the reduced cross-section (see Eq. (7)), arising from the exchange of longitudinally polarized photons, can be approximately or even less than a few percent, making it negligible within the considered kinematic range³.

Figures 6 and 7 warrant special attention. Fig. 6 shows the F_2 structure function as a function of Q^2 at various fixed x -values. Notably, we achieve excellent agreement with data for $x < 0.013$ ($\chi^2 = 1.10$) using both charm quark masses ($m_c = 1.4 \text{ GeV}$ and $m_c = 1.27 \text{ GeV}$). However, for the same x -values, the agreement weakens outside the fitting range ($Q^2 > 30 \text{ GeV}^2$). Fig. 7 demonstrates the description of F_2 data at low Q^2 values by our fits. Here, the agreement with experimental data is less satisfactory ($\chi^2 = 4.87$). This discrepancy might be related to the lack of a solid theoretical foundation for the wave functions at low Q^2 . As suggested in Ref. [48], incorporating a fixed value of $\bar{\alpha}_S = 0.2$ in the χ^2 calculation might potentially allow using the perturbative QCD wave function for the virtual photon even at relatively low Q^2 values. This approach warrants further investigation.

To expand the testing of the CGC/saturation NLO dipole model, we will now examine the exclusive diffractive processes at HERA. For the total cross-section, in Eq. (9) we performed the integral over $|t|$ up to 1 GeV^2 . In Figs. 9 and 10 we confront the experimental data from H1 and ZEUS with our theoretical predictions for Q^2 and W -dependence of the vector mesons J/ψ , ϕ and ρ production in different kinematics. We present our model results computed using two parameter sets from table I, which correspond to charm mass values of $m_c = 1.4 \text{ GeV}$ and $m_c = 1.27 \text{ GeV}$. These results are represented by solid and dashed lines, respectively. One can see that the agreement is excellent,

³ In our calculations, it was unnecessary to introduce an additional normalization factor between the light and charm sectors. For instance, in previous studies [68], the authors attempted this approach but encountered difficulties in accurately computing integrals over the impact parameter of a dipole. As explained on page 5, Section 2.4, they simply replaced these integrals with a constant value σ_0 . However, due to the distinct masses of charm and light quarks (resulting in different dipole sizes), such a substitution is evidently incorrect for all flavors, leading to discrepancies with data, particularly in the charm sector. In an effort to address this discrepancy, the authors introduced separate normalization constants σ_0 for the charm and light sectors. However, they expressed regret multiple times over this peculiar assumption, acknowledging that it undermines the dipole factorization picture. In contrast, this approach, as demonstrated in Refs. [45, 46, 48], achieves excellent agreement with data in both the light and charm sectors using only leading-order analysis. Consequently, introducing an additional normalization factor is unnecessary in this context.

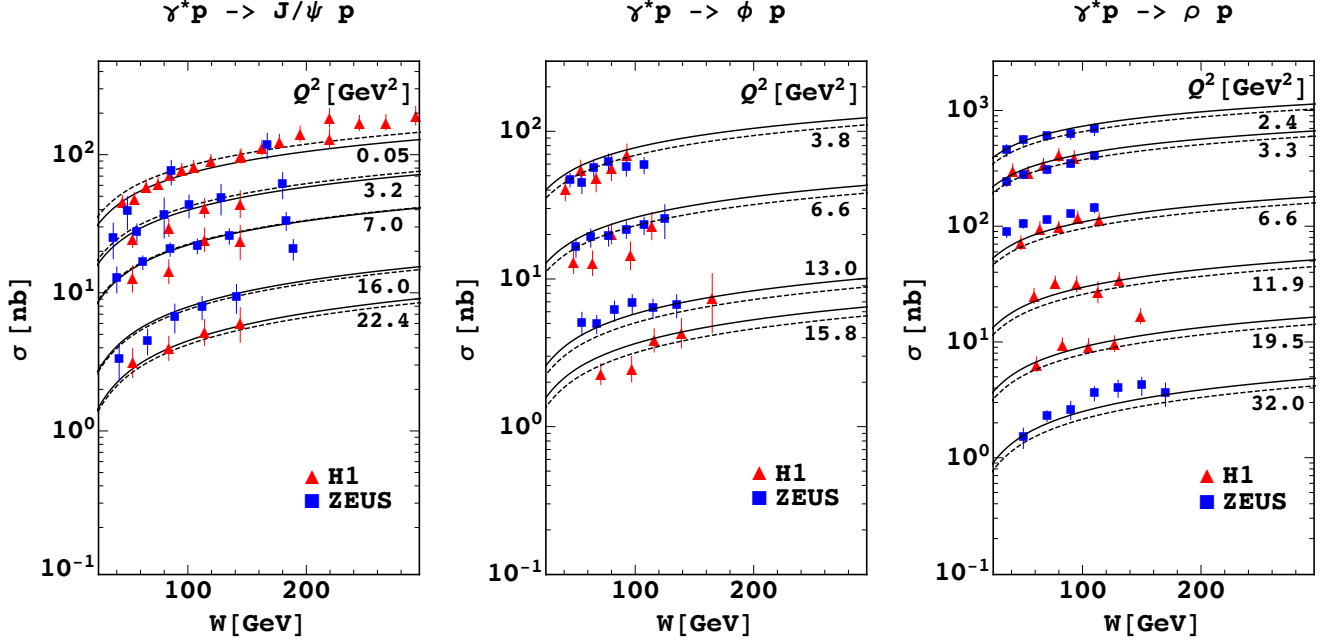


FIG. 10: Total vector meson cross-sections σ for J/ψ , ϕ and ρ , as a function of W . The solid lines correspond to parameters of set I ($m_c = 1.4$ GeV) and the dashed lines correspond to parameters of set II ($m_c = 1.27$ GeV). The data are from H1 and ZEUS collaborations [69–75].

particularly in the case of vector meson J/ψ , the wave function (specified in Eqs. (15), (16), and (17)) is proficient at replicating experimental data, even at lower values of $Q^2 + M_{J/\psi}^2$ (see Fig. 9). Notice that both parameter sets give similar estimates, however, for the case of vector meson J/ψ production, its total cross-section exhibits heightened sensitivity to the charm quark mass at low values of Q^2 (see Fig. 10) which differs from the behavior of lighter mesons ϕ and ρ . The reason for this lies in the fact that the scale in the integrand of the cross-section is established by ϵ_f as outlined in Eq. (5). It is only when virtualities are low, such as for $Q^2 < m_f^2$, that the cross-section starts to exhibit sensitivity to the quark mass.

In Table III we present the χ^2 values for each plot in the figures corresponding to the exclusive processes. Both sets of parameters provide a good description of the experimental data according to the χ^2 values. However, the diffractive production of the light meson ϕ deserves special attention. The χ^2 values for ϕ meson production are 2.48 for σ vs $Q^2 + M_\phi$ and 2.80 for σ vs W , suggesting a potential discrepancy between the theoretical predictions and the experimental measurements for this particular meson. This observation aligns with findings from previous studies (Refs. [45–47]), which also presented a similar situation in accurately predicting ϕ meson production data. Unfortunately, a direct comparison of χ^2 values across studies is not possible because the previous works did not report them.

The NLO dipole model can be applied to deeply inelastic Compton scattering (DVCS) with an accuracy comparable to other discussed reactions. However, limitations arise due to the procedures used to calculate the real part of the amplitude and its skewness can potentially affect the model’s ability to describe certain aspects of the data. These limitations are reflected in the χ^2 values obtained when comparing the model with experimental data. While the model provides reasonable agreement for the measured cross-sections, the predicted energy dependence of the cross-section’s slope deviates somewhat from the experimental data. Fig. 11 compares the NLO dipole model results with experimental data from the H1 and ZEUS collaborations [75, 76]. The left panel shows the dependence of the cross-section on Q^2 at fixed W values ($W = 82$ GeV and $W = 104$ GeV). This behavior is consistent for both parameter sets from Table I. The right panel presents the W -dependence of the cross-section for various fixed Q^2 values.

In Figs. 12 and 13 we present the ratio of the longitudinal to the transverse cross-sections $R = \sigma_L/\sigma_T$ for J/ψ , ϕ and ρ vector meson production as a function of Q^2 and W , respectively. One can predict that the ratio $R = \sigma_L/\sigma_T$

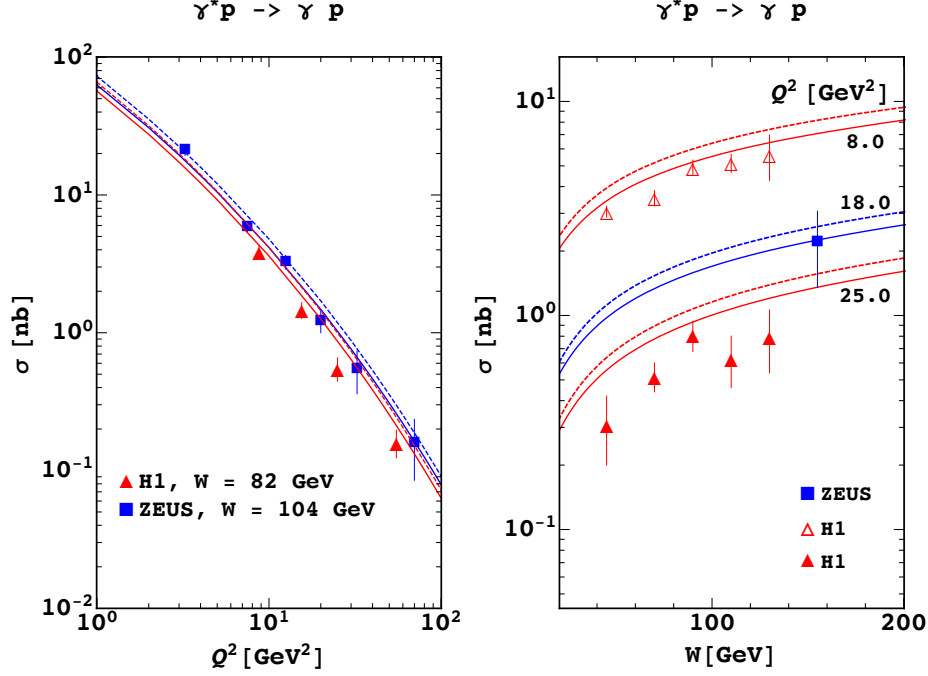


FIG. 11: Left: The Q^2 dependence of the cross section for DVCS. Right: The energy dependence of the cross section for DVCS. For theoretical results we use the parameters set given in table I $m_c = 1.4 \text{ GeV}$ in solid lines and $m_c = 1.27 \text{ GeV}$ in dashed lines. The data are from H1 and ZEUS collaborations [75, 76].

will exhibit an increase as Q^2 grows. This is because the ratio R conveys essential information about the effective average transverse size of the dipole involved in the interactions. Larger dipole sizes tend to predominantly influence the transverse component of the cross-section in contrast to the longitudinal component. Consequently, this results in a relative rise of the t -slope for the transverse component when compared to the longitudinal component. In Figure 12, our predictions were generated at a constant value of $W = 90 \text{ GeV}$, while the plot displays the range of W -bins in the experimental data. Nonetheless, the W dependency of the ratio remains notably weak under the condition of a fixed Q^2 [69–74]. Fig. 13 show that σ_L and σ_T exhibit identical dependencies on W , which are determined by the gluon distribution [60]. Consequently, the ratio remains constant. The weak dependence of R on W observed in this paper is consistent with both the MRT [60] and FS04 models [77].

Despite good χ^2 values for most plots in Table III for the longitudinal to transverse cross section ratio (R), the process R vs Q^2 for ρ meson production present an exception ($\chi^2 = 3.52$). This is expected due to: *i*) the influence of the dipole size on R , *ii*) differences in the saturation scale, and *iii*) internal factors of the model that influence the evolution of R such as dipole distribution, nonlinear effects, and the different parametrizations used. Focusing solely on the saturation scale, and comparing the values extracted from the CGC/saturation NLO dipole model with IP-Sat model (as shown in Figure 4 of Ref. [45]), reveals a crucial point. The IP-Sat model exhibits a larger contribution for very small- x values, including small impact parameters b , especially close to central collisions ($b \approx 0$). This trend is not observed when comparing the CGC/saturation NLO dipole model with the b-CGC saturation model [46] as we present in Figure 3. The CGC/saturation NLO dipole model's saturation scale exceeds the b-CGC model's scale, but only for very small- b values. Beyond $b > 2 \text{ GeV}^{-1}$, the b-CGC scale dominates. This variation in saturation scales directly affects dipole size, which in turn influences the transverse cross-section. Consequently, IP-Sat contributes more strongly to the transverse cross-section compared to the CGC/saturation NLO dipole model. This translates to a more pronounced curve for the CGC/saturation NLO dipole model compared to the one presented by the IP-Sat model. This explains the larger growth of R as a function of Q^2 for the ρ meson production.

Finally, results for the slope B_D of t -distribution of exclusive vector meson electroproduction and DVCS is presented in Figs. 14 and 15. One can see that the agreement of the model with the experimental data is reasonable. The slope B_D values for lighter vector mesons, at the same Q^2 , are higher than those for J/ψ vector meson production,

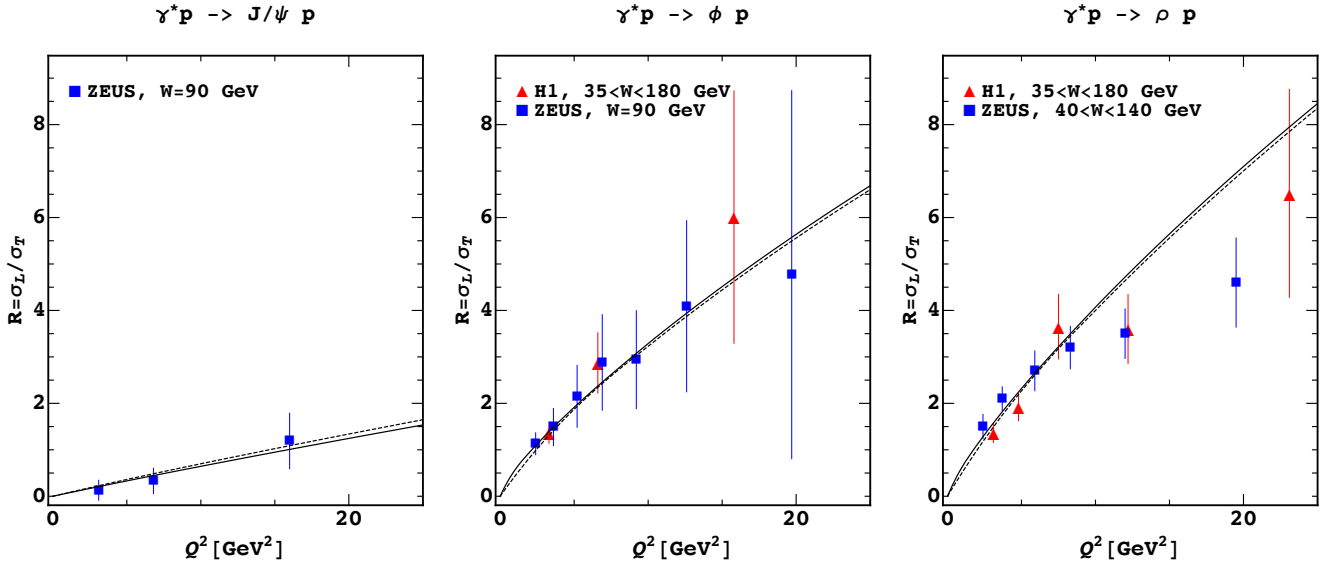


FIG. 12: The ratio $R = \sigma_L/\sigma_T$ for J/ψ , ϕ and ρ as a function of Q^2 . The solid ($m_c = 1.4$ GeV) and dashed ($m_c = 1.27$ GeV) lines correspond to parameter sets I and II, respectively. The experimental data are from H1 and ZEUS collaboration [69–74].

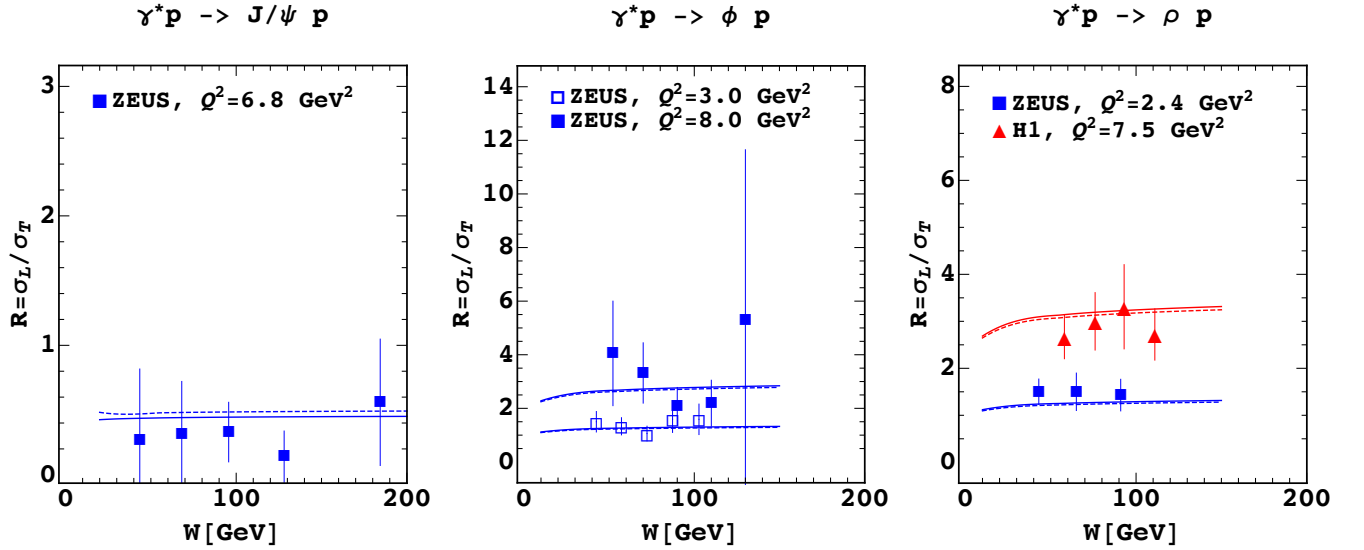


FIG. 13: The ratio $R = \sigma_L/\sigma_T$ for J/ψ , ϕ and ρ as a function of W . The solid and dashed lines are obtained using two distinct sets of parameters from table I corresponding to charm mass values of $m_c = 1.4, 1.27$ GeV, respectively. The experimental data are from H1 and ZEUS collaborations [69–74].

consistent with the experimental data. The reason for this lies in the convolution of the photon wavefunction with the vector meson wavefunction. It leads to different typical dipole sizes for light and heavy mesons, mainly determined by $1/\epsilon_f$ as described in equation Eq. (5). Hence, at a fixed virtuality, the typical dipole size is larger for lighter vector mesons, which, in turn, extends the range of validity for the asymptotic expression in Eq. (11) to higher Q^2 .

V. CONCLUSIONS

In this paper, we confronted the CGC/saturation NLO dipole model of Ref. [1] with the experimental combined HERA data, determining its parameters through the fitting procedure to the reduced inclusive DIS cross-section σ_r at small- x . Based on this approach, the re-summation procedure of Ref. [4–6] was included to fix the BFKL kernel in the

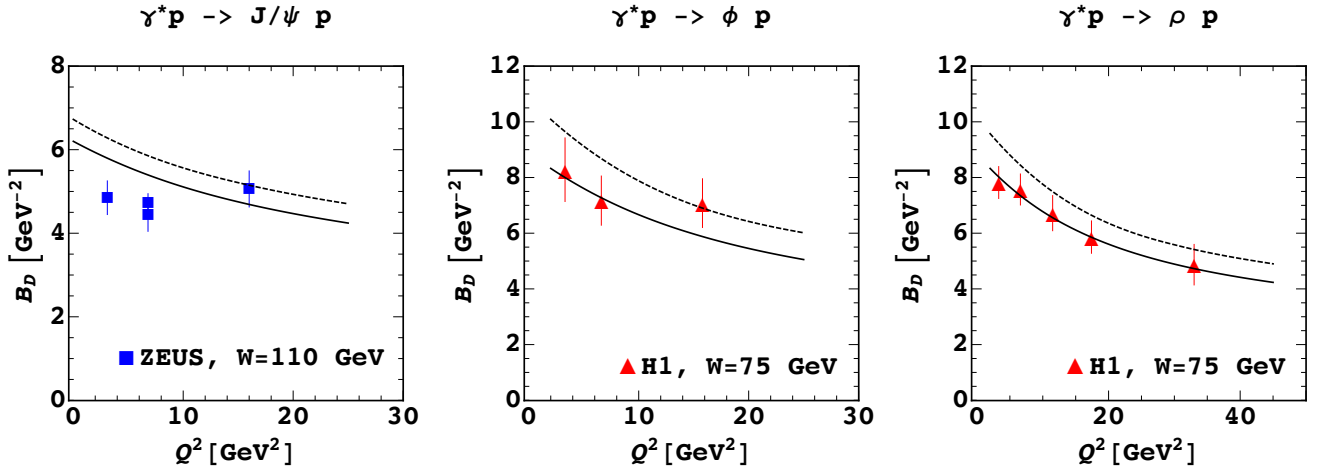


FIG. 14: Results for the slope B_D of t -distribution of exclusive vector meson electroproduction as a function of Q^2 . Solid and dashed lines represent calculations using charm quark masses of $m_c = 1.4$ GeV and $m_c = 1.27$ GeV, respectively, from table I. The collection of experimental data are from H1 and ZEUS collaboration [69–74].

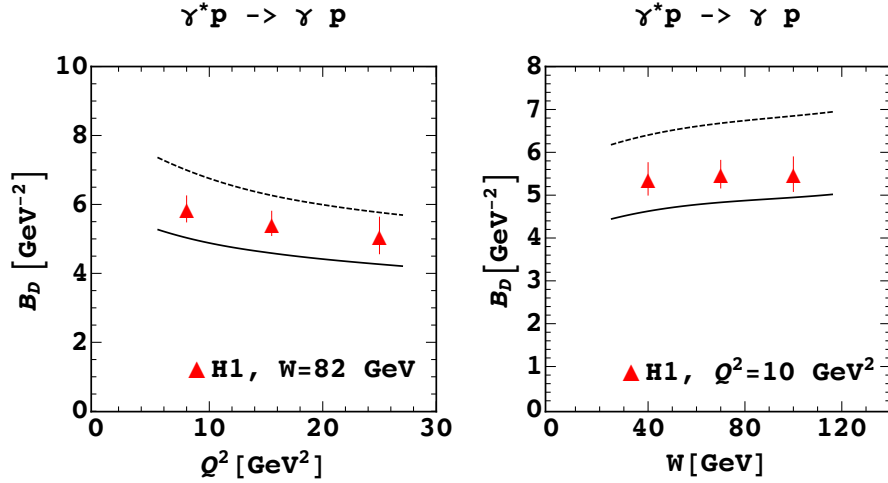


FIG. 15: Results for the slope B_D of t -distribution of DVCS processes as a function of Q^2 and W using parameters from table I. The solid line corresponds to $m_c = 1.4$ GeV, while the dashed line represents $m_c = 1.27$ GeV. The collection of experimental data are from H1 collaboration [76].

NLO, albeit with an alternative treatment of the nonlinear corrections which leads to additional change of the NLO kernel of the evolution equation. The model incorporates the NLO corrections not only deep within the saturation domain but also in the proximity of the saturation scale, as well as two essential ingredients: *i*) the correct solution to the non-linear BK evolution equation in the saturation region, and *ii*) the impact parameter distribution that results in an exponential decrease of the saturation momentum as the impact parameter b becomes large and a power-like decrease at high momentum transfers, in accordance with the principles of perturbative QCD. This approach differs from other attempts in that we employ $Q_s^2 \propto \exp(-mb)$ for large b , whereas in other models, Gaussian behavior at large b is assumed, with $Q_s^2 \propto \exp(-b^2/B)$. The exponential b dependence of Q_s^2 results in the exponential decrease of the scattering amplitude at large b , satisfying the Froissart theorem [21].

The model results are confronted to F_2 , F_2^{cc} , F_L , as well as for exclusive diffractive processes such as vector meson production and DVCS with the available data from HERA. Using four fitting parameters we obtain good overall agreement with the experimental data in the range $Q^2 \in [0.85, 120]$ GeV² and $x < 10^{-2}$. The extracted CGC/saturation NLO dipole model give the saturation scale for proton $Q_s^2 < 1$ GeV² in accord with other saturation models [45, 46]. It was illustrated that the CGC/saturation NLO dipole model provides an accurate representation of most aspects in both inclusive DIS and exclusive diffractive data, encompassing the Q^2 , W and x dependence. In

Figs. 4, 5, 8, 10 and 11, we extend our theoretical estimates outside the kinematics of existing data, as predictions for forthcoming DIS experiments. The slope B_D of t -distribution of exclusive vector meson electroproduction, including J/ψ , ϕ , ρ as well as DVCS can be correctly reproduced, even though the wave functions of the vector mesons and DVCS are quite different. This provides a strong indication of the consistency in the core dynamics and emphasizes the crucial nature of the impact parameter dependence in the saturation scale within the proton.

In contrast to b-CGC model, the NLO dipole model suffers from a high correlation between its four free parameters. To address this, one approach could involve introducing a fifth parameter, similar to the b-CGC model. This parameter could be set by fitting exclusive photoproduction data of a vector meson like J/ψ , potentially mitigating the correlation issue. Alternatively, this approach could also be explored by fitting the parameter m , using exclusive photoproduction data. However, further research is needed to clarify this conundrum and make the model more competitive on the market. Additionally, the model successfully replicates the experimental data for the ratio $R = \sigma_L/\sigma_T$. This observation bolsters the idea that the transverse dimensions of the dipole play a key role in determining the appropriate length scale for interactions with both transverse and longitudinally polarized virtual photons. While the CGC/saturation NLO dipole model exhibits good agreement with data for most processes, the case of the ρ meson production cross section R as a function of momentum squared Q^2 reveals a significant deviation. This discrepancy can be attributed to factors influencing the evolution of R , including dipole size and saturation scale variations. Our analysis across different models (IP-Sat, b-CGC, and CGC/saturation NLO) unveils a crucial connection between the saturation scales and R -evolution: the CGC/saturation NLO model's lower contribution for very small- x and b values leads to a more pronounced growth of R with increasing Q^2 for ρ meson production. This finding underscores the intricate interplay between saturation scales and cross-sectional behavior. Further investigations exploring the parameter space and incorporating these insights hold promise for a deeper understanding of high-energy parton saturation phenomena.

Our results provide a strong guide for finding an approach, based on Color Glass Condensate/saturation effective theory for high energy QCD, to make reliable predictions from first principles, as well as for upcoming DIS experiments. We believe that the model presented here, will be a useful tool to estimate the CGC/saturation effects in a variety of reactions, including the production of dijets in p-p and p-Pb collisions or the structure of the soft Pomeron in CGC. The model takes into account all the theoretical understanding we have regarding deep inelastic processes and, thus, can be used for comparisons at high energy. In summary, we firmly believe that this model is the only path forward based on solid theoretical ground to extending predictions to higher energy, including those present at the LHC.

VI. ACKNOWLEDGEMENTS

We thank our colleagues at UPLA and UTFSM for encouraging discussions, and for the use of computing infrastructure of the Scientific and Technological Center of Valparaiso, Universidad Técnica Federico Santa María (ANID PIA/APOYO AFB180002). Our special thanks go to M. Siddikov for all his suggestion on this paper. This work was supported by Plan de Fortalecimiento de Universidades Estatales, UPA 19101, CR 18.180, Código 2390, Universidad de Playa Ancha and ANID Grant No 3230699 (MR), and Grant PIIC N° 008/2023, DPP, Universidad Técnica Federico Santa María (JG).

* Electronic address: michael.roa@upla.cl

† Electronic address: jose.garridom@sansano.usm.cl

‡ Electronic address: miguel.guevara@upla.cl

- [1] C. Contreras, E. Levin, R. Meneses and M. Sanhueza, “Non-linear equation in the re-summed next-to-leading order of perturbative QCD: the leading twist approximation,” *Eur. Phys. J. C* **80** (2020) no.11, 1029 [arXiv:2007.06214 [hep-ph]].
- [2] J. Jalilian-Marian, A. Kovner, A. Leonidov and H. Weigert, *Phys. Rev.* **D59**, 014014 (1999), [arXiv:hep-ph/9706377]; *Nucl. Phys.* **B504**, 415 (1997), [arXiv:hep-ph/9701284]; J. Jalilian-Marian, A. Kovner and H. Weigert, *Phys. Rev.* **D59**, 014015 (1999), [arXiv:hep-ph/9709432]; A. Kovner, J. G. Milhano and H. Weigert, *Phys. Rev.* **D62**, 114005 (2000), [arXiv:hep-ph/0004014]; E. Iancu, A. Leonidov and L. D. McLerran, *Phys. Lett.* **B510**, 133 (2001); [arXiv:hep-ph/0102009]; *Nucl. Phys.* **A692**, 583 (2001), [arXiv:hep-ph/0011241]; E. Ferreiro, E. Iancu, A. Leonidov and L. McLerran, *Nucl. Phys.* **A703**, 489 (2002), [arXiv:hep-ph/0109115]; H. Weigert, *Nucl. Phys.* **A703**, 823 (2002), [arXiv:hep-ph/0004044].
- [3] I. Balitsky, [arXiv:hep-ph/9509348]; *Phys. Rev.* **D60**, 014020 (1999) [arXiv:hep-ph/9812311]; Y. V. Kovchegov, *Phys. Rev.* **D60**, 034008 (1999), [arXiv:hep-ph/9901281].
- [4] G. P. Salam, “A Resummation of large subleading corrections at small x ,” *JHEP* **9807** (1998) 019 [hep-ph/9806482];

- [5] M. Ciafaloni, D. Colferai and G. P. Salam, “Renormalization group improved small x equation,” Phys. Rev. D **60** (1999) 114036 [hep-ph/9905566].
- [6] M. Ciafaloni, D. Colferai, G. P. Salam and A. M. Stasto, “Renormalization group improved small x Green’s function,” Phys. Rev. D **68** (2003) 114003, [hep-ph/0307188].
- [7] B. Ducloué, E. Iancu, A. H. Mueller, G. Soyez and D. N. Triantafyllopoulos, JHEP **04**, 081 (2019) [arXiv:1902.06637 [hep-ph]].
- [8] V. S. Fadin, E. A. Kuraev and L. N. Lipatov, “On the pomeron singularity in asymptotically free theories”, Phys. Lett. **B60**, 50 (1975); E. A. Kuraev, L. N. Lipatov and V. S. Fadin, “The Pomeron singularity in Nonabelian Gauge Theories” Sov. Phys. JETP **45**, 199 (1977), [Zh. Eksp. Teor. Fiz.72,377(1977)]; I. I. Balitsky and L. N. Lipatov, “The Pomeron singularity in Quantum Chromodynamics,” Sov. J. Nucl. Phys. **28**, 822 (1978), [Yad. Fiz.28,1597(1978)].
- [9] L. N. Lipatov, “Small x physics in perturbative QCD,” Phys. Rept. **286**, 131 (1997) [hep-ph/9610276]; “The Bare Pomeron in Quantum Chromodynamics,” Sov. Phys. JETP **63**, 904 (1986) [Zh. Eksp. Teor. Fiz. **90**, 1536 (1986)].
- [10] E. Levin and K. Tuchin, “Solution to the evolution equation for high parton density QCD,” Nucl. Phys. **B573**, 833 (2000) [hep-ph/9908317]; “New scaling at high-energy DIS,” Nucl. Phys. **A691**, 779 (2001) [hep-ph/0012167]; “Nonlinear evolution and saturation for heavy nuclei in DIS,” **693**, 787 (2001) [hep-ph/0101275].
- [11] C. Contreras, E. Levin, R. Meneses and I. Potashnikova, “CGC/saturation approach: a new impact-parameter dependent model in the next-to-leading order of perturbative QCD,” Phys. Rev. D **94**, no.11, 114028 (2016) [arXiv:1607.00832 [hep-ph]].
- [12] W. Xiang, Y. Cai, M. Wang and D. Zhou, “Rare fluctuations of the S-matrix at NLO in QCD,” Phys. Rev. **D99** (2019) no.9, 096026 [arXiv:1812.10739 [hep-ph]].
- [13] I. Balitsky, “Quark contribution to the small- x evolution of color dipole,” Phys. Rev. D **75** (2007) 014001, [hep-ph/0609105].
- [14] Y. V. Kovchegov and H. Weigert, “Triumvirate of Running Couplings in Small- x Evolution,” Nucl. Phys. **A784** (2007) 188, [hep-ph/0609090].
- [15] I. Balitsky and G. A. Chirilli, “Next-to-leading order evolution of color dipoles”, Phys. Rev. **D77** (2008) 014019 [arXiv:0710.4330 [hep-ph]].
- [16] I. Balitsky and G. A. Chirilli, “Rapidity evolution of Wilson lines at the next-to-leading order”, Phys. Rev. **D88** (2013) 111501, [arXiv:1309.7644 [hep-ph]].
- [17] A. Kovner, M. Lublinsky, and Y. Mulian, “Jalilian-Marian, Iancu, McLerran, Weigert, Leonidov, Kovner evolution at next to leading order”, Phys. Rev. **D89** (2014) no. 6, 061704, [arXiv:1310.0378 [hep-ph]].
- [18] A. Kovner, M. Lublinsky, and Y. Mulian, “NLO JIMWLK evolution unabridged”, JHEP **08** (2014) 114, [arXiv:1405.0418 [hep-ph]].
- [19] M. Lublinsky and Y. Mulian, “High Energy QCD at NLO: from light-cone wave function to JIMWLK evolution”, JHEP **05** (2017) 097, [arXiv:1610.03453 [hep-ph]].
- [20] Yuri V Kovchegov and Eugene Levin, “Quantum Chromodynamics at High Energies”, Cambridge Monographs on Particle Physics, Nuclear Physics and Cosmology, Cambridge University Press, 2012 .
- [21] M. Froissart, *Phys. Rev.* **123** (1961) 1053;
A. Martin, “Scattering Theory: Unitarity, Analyticity and Crossing.” Lecture Notes in Physics, Springer-Verlag, Berlin-Heidelberg-New-York, 1969.
- [22] A. Kovner and U. A. Wiedemann, Phys. Rev. D **66**, 051502 (2002) [hep-ph/0112140]; Phys. Rev. D **66**, 034031 (2002) [hep-ph/0204277]; Phys. Lett. B **551**, 311 (2003) [hep-ph/0207335].
- [23] E. Ferreira, E. Iancu, K. Itakura and L. McLerran, “Froissart bound from gluon saturation,” Nucl. Phys. **A710**, 373 (2002) [hep-ph/0206241].
- [24] J. Bartels, E. Levin, Nucl. Phys. **B387** (1992) 617-637; L. McLerran, M. Praszalowicz, Acta Phys. Polon. **B42** (2011) 99, [arXiv:1011.3403 [hep-ph]] **B41** (2010) 1917-1926, [arXiv:1006.4293 [hep-ph]]; M. Praszalowicz, Acta Phys. Polon. B **42** (2011) 1557 [arXiv:1104.1777 [hep-ph]]; M. Praszalowicz and T. Stebel, JHEP **1303** (2013) 090 [arXiv:1211.5305 [hep-ph]]; L. McLerran, M. Praszalowicz and B. Schenke, Nucl. Phys. A **916** (2013) 210 [arXiv:1306.2350 [hep-ph]]; M. Praszalowicz, Phys. Lett. B **727** (2013) 461 [arXiv:1308.5911 [hep-ph]]; L. McLerran and M. Praszalowicz, Phys. Lett. B **741** (2015) 246 [arXiv:1407.6687 [hep-ph]].
- [25] A. M. Stasto, K. J. Golec-Biernat, J. Kwiecinski, “Geometric scaling for the total gamma* p cross-section in the low x region,” Phys. Rev. Lett. **86** (2001) 596-599, [hep-ph/0007192].
- [26] S. Bondarenko, M. Kozlov and E. Levin, “QCD saturation in the semi-classical approach,” Nucl. Phys. **A727** (2003), 139-178 [arXiv:hep-ph/0305150 [hep-ph]].
- [27] K. J. Golec-Biernat and M. Wusthoff, “Saturation in diffractive deep inelastic scattering,” Phys. Rev. **D60** (1999) 114023 [hep-ph/9903358]; “Saturation effects in deep inelastic scattering at low Q^2 and its implications on diffraction,” Phys. Rev. **D59** (1998) 014017; [hep-ph/9807513].
- [28] J. Berger and A. M. Stasto, “Small x nonlinear evolution with impact parameter and the structure function data,” Phys. Rev. D **84** (2011), 094022 [arXiv:1106.5740 [hep-ph]].
- [29] J. Bartels, K. J. Golec-Biernat and H. Kowalski, “A modification of the saturation model: DGLAP evolution,” Phys. Rev. **D66** (2002) 014001 [hep-ph/0203258].
- [30] H. Kowalski and D. Teaney, “An Impact parameter dipole saturation model,” Phys. Rev. **D68** (2003) 114005 [hep-ph/0304189].
- [31] E. Iancu, K. Itakura and S. Munier, “Saturation and BFKL dynamics in the HERA data at small x,” Phys. Lett. **B590** (2004) 199 [hep-ph/0310338].
- [32] H. Kowalski, L. Motyka and G. Watt, “Exclusive diffractive processes at HERA within the dipole picture,” Phys. Rev. **D74** (2006) 074016 [hep-ph/0606272].

- [33] H. Kowalski, T. Lappi and R. Venugopalan, “Nuclear enhancement of universal dynamics of high parton densities,” *Phys. Rev. Lett.* **100** (2008) 022303 [arXiv:0705.3047 [hep-ph]].
- [34] H. Kowalski, T. Lappi, C. Marquet and R. Venugopalan, “Nuclear enhancement and suppression of diffractive structure functions at high energies,” *Phys. Rev.* **C78** (2008) 045201 [arXiv:0805.4071 [hep-ph]].
- [35] G. Watt and H. Kowalski, “Impact parameter dependent colour glass condensate dipole model,” *Phys. Rev.* **D78** (2008) 014016 [arXiv:0712.2670 [hep-ph]].
- [36] E. Levin and A. H. Rezaeian, “Gluon saturation and inclusive hadron production at LHC,” *Phys. Rev.* **D82** (2010) 014022 [arXiv:1005.0631 [hep-ph]].
- [37] A. H. Rezaeian, “CGC predictions for $p+A$ collisions at the LHC and signature of QCD saturation,” *Phys. Lett.* **B718** (2013) 1058 [arXiv:1210.2385 [hep-ph]].
- [38] E. Levin and A. H. Rezaeian, “Gluon saturation and energy dependence of hadron multiplicity in pp and AA collisions at the LHC,” *Phys. Rev.* **D83** (2011) 114001 [arXiv:1102.2385 [hep-ph]].
- [39] E. Levin and A. H. Rezaeian, “Hadron multiplicity in pp and AA collisions at LHC from the Color Glass Condensate,” *Phys. Rev.* **D82** (2010) 054003 [arXiv:1007.2430 [hep-ph]].
- [40] D. Boer, M. Diehl, R. Milner, R. Venugopalan, W. Vogelsang, D. Kaplan, H. Montgomery and S. Vigdor *et al.*, “Gluons and the quark sea at high energies: Distributions, polarization, tomography,” [arXiv:1108.1713 [nucl-th]].
- [41] T. Lappi and H. Mantysaari, “Incoherent diffractive J/Ψ -production in high energy nuclear DIS,” *Phys. Rev.* **C83** (2011) 065202 [arXiv:1011.1988 [hep-ph]].
- [42] T. Toll and T. Ullrich, “Exclusive diffractive processes in electron-ion collisions,” *Phys. Rev.* **C87** (2013) 2, 024913 [arXiv:1211.3048 [hep-ph]].
- [43] P. Tribedy and R. Venugopalan, “Saturation models of HERA DIS data and inclusive hadron distributions in $p+p$ collisions at the LHC,” *Nucl. Phys.* **A850** (2011) 136 [Nucl. Phys. A **859** (2011) 185] [arXiv:1011.1895 [hep-ph]].
- [44] P. Tribedy and R. Venugopalan, “QCD saturation at the LHC: comparisons of models to $p+p$ and $A+A$ data and predictions for $p+Pb$ collisions,” *Phys. Lett.* **B710** (2012) 125 [Phys. Lett. **B718** (2013) 1154] [arXiv:1112.2445 [hep-ph]].
- [45] A. H. Rezaeian, M. Siddikov, M. Van de Klundert and R. Venugopalan, “IP-Sat: Impact-Parameter dependent Saturation model revised,” *PoS DIS 2013* (2013) 060 [arXiv:1307.0165 [hep-ph]]; “Analysis of combined HERA data in the Impact-Parameter dependent Saturation model,” *Phys. Rev.* **D87** (2013) 3, 034002 [arXiv:1212.2974].
- [46] A. H. Rezaeian and I. Schmidt, “Impact-parameter dependent Color Glass Condensate dipole model and new combined HERA data,” *Phys. Rev.* **D88** (2013) 074016 [arXiv:1307.0825 [hep-ph]].
- [47] C. Contreras, E. Levin and I. Potashnikova, “CGC/saturation approach: a new impact-parameter dependent model,” *Nucl. Phys.* **A948** (2016), 1-18 [arXiv:1508.02544 [hep-ph]].
- [48] C. Contreras, E. Levin and M. Sanhueza, “Non-linear evolution in the re-summed next-to-leading order of perturbative QCD: confronting the experimental data,” [arXiv:2106.06214 [hep-ph]].
- [49] G. P. Lepage and S. J. Brodsky, *Phys. Rev. Lett.* **43** (1979) 545; *Phys. Rev. Lett.* **43** (1979) 1625.
- [50] F. D. Aaron *et al.* [H1 and ZEUS Collaborations], “Combined Measurement and QCD Analysis of the Inclusive ep Scattering Cross Sections at HERA,” *JHEP* **1001** (2010) 109 [arXiv:0911.0884 [hep-ex]].
- [51] H. Abramowicz *et al.* [H1 and ZEUS Collaborations], “Combination and QCD Analysis of Charm Production Cross Section Measurements in Deep-Inelastic ep Scattering at HERA,” *Eur. Phys. J. C* **73** (2013) 2, 2311 [arXiv:1211.1182 [hep-ex]].
- [52] D. Boer, M. Diehl, R. Milner, R. Venugopalan, W. Vogelsang, D. Kaplan, H. Montgomery, S. Vigdor, A. Accardi and E. C. Aschenauer, *et al.* [arXiv:1108.1713 [nucl-th]]; R. Abdul Khalek, U. D’Alesio, M. Arratia, A. Bacchetta, M. Battaglieri, M. Begel, M. Boglione, R. Boughezal, R. Boussarie and G. Bozzi, *et al.* [arXiv:2203.13199 [hep-ph]].
- [53] J. L. Abelleira Fernandez *et al.* [LHeC Study Group], *J. Phys. G* **39** (2012), 075001 [arXiv:1206.2913 [physics.acc-ph]].
- [54] K. Kutak and S. Sapeta, *Phys. Rev. D* **86** (2012), 094043 [arXiv:1205.5035 [hep-ph]].
- [55] C. Contreras, E. Levin and M. Sanhueza, “Soft pomeron in the color glass condensate approach,” *Phys. Rev. D* **106** (2022) no.3, 034011 [arXiv:2203.10296 [hep-ph]].
- [56] J. Bartels, K. Golec-Biernat and K. Peters, “On the Dipole Picture in the Nonforward Direction,” *Acta Phys. Polon.* **B34**, 3051 (2003)
- [57] Y. Hatta, B. W. Xiao and F. Yuan, “Gluon Tomography from Deeply Virtual Compton Scattering at Small- x ,” *Phys. Rev. D* **95**, no.11, 114026 (2017) doi:10.1103/PhysRevD.95.114026 [arXiv:1703.02085 [hep-ph]].
- [58] E. Gotsman, E. M. Levin and U. Maor, *Z. Phys. C* **57** (1993), 677-684 [arXiv:hep-ph/9209218 [hep-ph]].
- [59] J. Nemchik, N. N. Nikolaev and B. G. Zakharov, *Phys. Lett. B* **341** (1994), 228-237 [arXiv:hep-ph/9405355 [hep-ph]]; J. Nemchik, N. N. Nikolaev, E. Predazzi and B. G. Zakharov, *Z. Phys. C* **75** (1997), 71-87 [arXiv:hep-ph/9605231 [hep-ph]]; J. R. Forshaw, R. Sandapen and G. Shaw, *Phys. Rev. D* **69** (2004), 094013 [arXiv:hep-ph/0312172 [hep-ph]].
- [60] A. D. Martin, M. G. Ryskin and T. Teubner, *Phys. Rev. D* **62** (2000), 014022 [arXiv:hep-ph/9912551 [hep-ph]].
- [61] A. G. Shuvaev, K. J. Golec-Biernat, A. D. Martin and M. G. Ryskin, *Phys. Rev. D* **60** (1999), 014015 [arXiv:hep-ph/9902410 [hep-ph]].
- [62] E. Levin, “Dipole-dipole scattering in CGC/saturation approach at high energy: summing Pomeron loops,” *JHEP* **11** (2013), 039 [arXiv:1308.5052 [hep-ph]].
- [63] E. Iancu, K. Itakura and L. McLerran, “Geometric scaling above the saturation scale,” *Nucl. Phys.* **A708** (2002) 327 [hep-ph/0203137].
- [64] H. Mäntysaari and P. Zurita, *Phys. Rev. D* **98** (2018), 036002 [arXiv:1804.05311 [hep-ph]].
- [65] B. Sambasivam, T. Toll and T. Ullrich, *Phys. Lett. B* **803** (2020), 135277 [arXiv:1910.02899 [hep-ph]].
- [66] H. Abramowicz *et al.* [ZEUS Collaboration], “Deep inelastic cross-section measurements at large y with the ZEUS detector at HERA,” *Phys. Rev.* **D90** (2014) 7, 072002 [arXiv:1404.6376 [hep-ex]]; S. Chekanov *et al.* [ZEUS Collaboration],

- “Measurement of the Longitudinal Proton Structure Function at HERA,” Phys. Lett. **B682** (2009) 8 [arXiv:0904.1092 [hep-ex]].
- [67] V. Andreev *et al.* [H1], “Measurement of inclusive ep cross sections at high Q^2 at $\sqrt{s} = 225$ and 252 GeV and of the longitudinal proton structure function F_L at HERA,” Eur. Phys. J. C **74**, no.4, 2814 (2014) [arXiv:1312.4821 [hep-ex]].
- [68] J. L. Albacete, N. Armesto, J. G. Milhano, P. Quiroga-Arias and C. A. Salgado, Eur. Phys. J. C **71** (2011), 1705 [arXiv:1012.4408 [hep-ph]].
- [69] S. Chekanov *et al.* [ZEUS], PMC Phys. A **1**, 6 (2007) [arXiv:0708.1478 [hep-ex]].
- [70] S. Chekanov *et al.* [ZEUS], Eur. Phys. J. C **24**, 345-360 (2002) [arXiv:hep-ex/0201043 [hep-ex]].
- [71] S. Chekanov *et al.* [ZEUS], Nucl. Phys. B **695**, 3-37 (2004) [arXiv:hep-ex/0404008 [hep-ex]].
- [72] A. Aktas *et al.* [H1], Eur. Phys. J. C **46**, 585-603 (2006) [arXiv:hep-ex/0510016 [hep-ex]].
- [73] S. Chekanov *et al.* [ZEUS], Nucl. Phys. B **718**, 3-31 (2005) [arXiv:hep-ex/0504010 [hep-ex]].
- [74] F. D. Aaron *et al.* [H1], JHEP **05**, 032 (2010) [arXiv:0910.5831 [hep-ex]].
- [75] S. Chekanov *et al.* [ZEUS], JHEP **05**, 108 (2009) [arXiv:0812.2517 [hep-ex]].
- [76] F. D. Aaron *et al.* [H1], Phys. Lett. B **681**, 391-399 (2009) [arXiv:0907.5289 [hep-ex]]; S. Chekanov *et al.* [ZEUS Collaboration], PMC Phys. **A1**, 6 (2007), [arXiv:0812.2517 [hep-ex]].
- [77] J. R. Forshaw and G. Shaw, JHEP **12** (2004), 052 [arXiv:hep-ph/0411337 [hep-ph]].